Goddard Space
IN-25-CR
142329
568

Progress Report to National Aeronautics and Space Administration (NASA)
Greenbelt, MD 20071

NAG 5-526

Theoretical Studies of Resonance Enhanced Stimulated Raman Scattering (RESRS) of Frequency-Doubled Alexandrite Laser Wavelength in Cesium Vapor

Principal Investigator
Nabil M. Lawandy
Associate Professor of Engineering and Physics
Brown University
Providence, RI 02912

January-June, 1987

(NASA-CR-182870) THEORETICAL STUDIES OF RESONANCE ENHANCED STIMULATED RAMAN SCATTERING (RESRS) OF FREQUENCY-DOUBLED ALEXANDRITE LASER WAVELENGTH IN CESIUM VAPOR Progress Report, Jan. - Jun. 1987 (Brown
N88-22133
Unclas
G3/25 0142329

Progress Report

The work during this period was aimed at elucidating the effects of a velocity distribution on the RERS process. The particular case of Cs vapor was investigated. The results of this work are best summarized in the publication preprint which follows. This paper was submitted to the Journal of Applied Physics B.

MULTIPLE RELAXATION AND INHOMOGENEOUS BROADENING IN RESONANCE ENHANCED RAMAN SCATTERING: APPLICATION TO TUNABLE INFRARED GENERATION

by

John C. Ryan* and Nabil M. Lawandy†

*Department of Physics
†Division of Engineering and Department of Physics
Brown University
Providence, Rhode Island 02912

Abstract

The solutions for the imaginary susceptibility of the Raman field transition with arbitrary relaxation rates and field strengths are examined for three different sets of relaxation rates. These rates correspond to (1) Far infrared (FIR) Raman lasers in the diabatic collision regime without consideration of coupled population decay in a closed system, (2) Raman FIR lasers in the diabatic collision regime with coupled population conserving decay, and (3) IR Raman gain in cesium vapor. The model is further expanded to include Doppler broadening and used to predict the peak gain as a function of detuning for a frequency doubled alexandrite laser-pumped cesium vapor gain cell.

This work was supported by an Alfred P. Sloan Fellowship and a grant from the National Aeronautics and Space Administration (NAG-5-526).

Introduction

In this paper we consider the gain in a coherently pumped three level system by examining solutions of the density matrix calculation with arbitrary relaxation rates, field strengths, and detunings.[1]

The problem of a three level laser was first examined quantum mechanically by Javan.[2] However, his solution is valid only for a weak stimulated field, or for equal pump and stimulated field detuning in the strong field case. Many other authors[3,4,5,6] have examined the three level system with various approximations, most notably Panock and Temkin[6] whose solution is applicable for arbitrarily strong pump and stimulated fields, but assumes all relaxation rates to be equal. These solutions are necessary for the description of resonance enhanced Raman techniques for generating tunable radiation. Tunable radiation has been obtained using tunable pump lasers and various gases in the far infrared and near infrared regions of the spectrum. The far infrared systems utilized CO_2 TEA lasers as tunable pumps and molecular gases such as CH_3F. The infrared systems were based around tunable dye laser pumps and atomic vapors such as the alkali metals. The recent development of the tunable alexandrite laser and efficient frequency doubling and tripling crystals has made possible solid state laser pumped alkali metal vapor infrared systems.

In Section I we present the model used to approximate the gain in a coherently pumped three level system and the basis of the calculation of the susceptibilities. In Section II we examine the effects of different relaxation rates on the homogeneous line shape including how the various contributing terms in the imaginary stimulated susceptibility saturate with stimulated field intensity.

In Section III the model is expanded to include Doppler broadening. We then briefly examine some of the properties of the Doppler broadened line shape and show that although the results at low pump power and detuning within the Doppler width agree with the previous calculation,[7,8] the line shape for large pump fields and

detunings outside of the Doppler width does not reduce to the homogeneous case. We then apply the inhomogeneous model to a doubled alexandrite pumped cesium vapor laser in order to study stimulated infrared Raman emission. Much of the present theory of stimulated Raman emission in non-linear optics is based on calculations of $\chi^{(3)}$ from second order perturbation theory.[9,10,11] This approach neglects many important effects of the complicated population dynamics associated with the relaxation processes of any multi-level quantum system. It is also shown that the Doppler broadened prediction of stimulated gain with tuning differs significantly from the homogeneous prediction.

I. Theory

We have modeled coherently pumped atomic and molecular lasers of a three-level system in an "inverted V" configuration, shown in Fig. 1. The complex susceptibilities were obtained[1] using the density matrix formalism while neglecting all non-resonant terms in the interaction picture. This treatment differs from others[2,3,4,5,6] in that both arbitrary longitudinal and transverse rates as well as arbitrary field strengths are allowed. The system is assumed to be closed so that there is no net loss of probability.

The zero field rate of decay of the average probability in any state will depend upon the configuration of the entire system and not only upon the value of the probability in that particular state. For instance, if the system in Figure 1 was prepared in a configuration in which the ensemble averaged probability of finding the system in state $|2\rangle$ was equal to its thermal equilibrium value while that of state $|3\rangle$ were greater than its thermal equilibrium value, state $|2\rangle$ will not remain in equilibrium, since one channel of decay for state $|3\rangle$ is through state $|2\rangle$. Therefore, there will be an increase in the probability of finding the system in state $|2\rangle$. It is clear then that any one state willl retain its equilibrium probability only if the <u>entire</u> system is in equilibrium. Rates of decrease or increase of probability in the zero field case can only be defined between level pairs so that when fields are present the time dependence of the diagonal elements are governed by

$$\dot{\rho}_{11} = \frac{-i}{\hbar}(\mu_{31}\rho_{13} - \mu_{13}\rho_{31})\cdot\vec{E}(t) - \frac{1}{T_1}(f_{31}\rho_{11} - \rho_{33}) - \frac{1}{T_3}(f_{21}\rho_{11} - \rho_{22}) \quad (1)$$

$$\dot{\rho}_{22} = \frac{-i}{\hbar}(\mu_{32}\rho_{23} - \mu_{23}\rho_{32})\cdot\vec{E}(t) - \frac{1}{T_1}(f_{32}\rho_{22} - \rho_{33}) - \frac{1}{T_3}(\rho_{22} - f_{21}\rho_{11}) \quad (2)$$

$$\dot{\rho}_{33} = \frac{i}{\hbar}\left[(\mu_{31}\rho_{13} - \mu_{13}\rho_{31}) + (\mu_{23}\rho_{32} - \mu_{32}\rho_{23})\right]\cdot\vec{E}(t) - \frac{1}{T_1}(\rho_{33} - f_{32}\rho_{22}) - \frac{1}{T_2}(\rho_{33} - f_{31}\rho_{11}) \quad (3)$$

where the f_{ij}'s are equilibrium occupation ratios (ratio of i^{th} to j^{th} equilibrium population), and T_1, T_2, and T_3 are the spectroscopically measured relaxation rates of the specified level pairs. Notice that $tr\dot{\rho} = 0$ is satisfied identically, showing probability conservation.

Rewriting Eqs. (1-3) in terms of the population differences $\Delta_{13} = \rho_{11} - \rho_{33}$ and $\Delta_{32} = \rho_{33} - \rho_{22}$ and $Tr\rho = 1$, we have

$$\dot{\Delta}_{13} = \frac{-1}{\hbar} \mathrm{Im}\ [\mu_{23}\sigma_{31}Es] + \frac{2}{\hbar}\ \mathrm{Im}[\mu_{31}\sigma_{13}E_p^*]$$

$$-k_1\,[\,(\Delta_{13} - \Delta_{13}^0)] + k_2\,[(\Delta_{32} - \Delta_{32}^0)] \qquad (4)$$

$$\dot{\Delta}_{32} = \frac{-1}{\hbar}\,\mathrm{Im}\ [\mu_{31} - \sigma_{13}E_p^*] + \frac{2}{\hbar}\,\mathrm{Im}[\mu_{23}\sigma_{32}E_s] + k_3[(\Delta_{13} - \Delta_{13}^0)] - k_4[(\Delta_{32} - \Delta_{32}^0)] \qquad (5)$$

where σ_{ij} are the density matrix elements in the interaction picture. E_s and E_p are the complex amplitudes of the signal and pump fields and the constants k_1, k_2, k_3, k_4,Δ_{32}^0 and Δ_{32}^0 are defined in terms of T_1, T_2, T_3 and f_{ij} by the following relations.

$$k_1 = \frac{1}{3}\left[\frac{1 - f_{32}}{T_1} + \frac{2 + 4f_{31}}{T_2} + \frac{1 + 2f_{21}}{T_3}\right] \qquad (6)$$

$$k_2 = \frac{1}{3}\left[\frac{1 + 2f_{32}}{T_1} + \frac{2 - 2f_{31}}{T_2} - \frac{2 + f_{21}}{T_3}\right] \qquad (7)$$

$$k_3 = \frac{1}{3}\left[\frac{2 - 2f_{32}}{T_1} + \frac{1 + 2f_{31}}{T_2} + \frac{1 + f_{21}}{T_3}\right] \qquad (8)$$

$$k_4 = \frac{1}{3}\left[\frac{2 + 4f_{32}}{T_1} \quad \frac{1 - f_{31}}{T_2} \quad \frac{2 + f_{21}}{T_3}\right] \tag{9}$$

$$\Delta_{13}^0 = \frac{1 - f_{31}}{1 + f_{21} + f_{31}} \tag{10}$$

$$\Delta_{32}^0 = \frac{f_{31} - f_{21}}{1 + f_{21} + f_{31}} \tag{11}$$

The off diagonal elements, on the other hand, give the average amplitude mixing between level pairs. The zero field decay of these elements can be approximated to first order by a simple exponential decay without contradiction.[12]

The resulting susceptibilities are given by:

$$\chi_p'' = \frac{-|\mu_{13}|^2}{\hbar(\delta_p^2 + \tau_2^{-2})}\left\{\Delta_{13}\left[\tau_2^{-1} - \frac{|\beta_s|^2\alpha_1}{(\delta_p^2 + \tau_2^{-2})}\right] + \Delta_{32}\frac{|\beta_s|^2\alpha_2}{(\delta_s^2 + \tau_1^{-2})}\right\} \tag{12}$$

$$\chi_s'' = \frac{|\mu_{32}|^2}{\hbar(\delta_s^2 + \tau_1^{-2})}\left\{\Delta_{32}\left[\tau_1^{-1} + \frac{|\beta_p|^2\alpha_3}{(\delta_s^2 + \tau_1^{-2})}\right] + \Delta_{13}\frac{|\beta_p|^2\alpha_2}{(\delta_p^2 + \tau_2^{-2})}\right\} \tag{13}$$

$$\chi_p' = \frac{-|\mu_{13}|^2}{\hbar(\delta_p^2 + \tau_2^{-2})}\left\{\Delta_{13}\left[\delta_p^{-1} - \frac{|\beta_s|^2\gamma_1}{(\delta_p^2 + \tau_2^{-2})}\right] - \Delta_{32}\frac{|\beta_s|^2\gamma_2}{(\delta_s^2 + \tau_1^{-2})}\right\} \tag{14}$$

$$\chi_p' = \frac{|\mu_{32}|^2}{\hbar(\delta_s^2 + \tau_1^{-2})}\left\{\Delta_{32}\left[\delta_s + \frac{|\beta_p|^2\gamma_3}{(\delta_s^2 + \tau_1^{-2})}\right] + \Delta_{13}\frac{|\beta_p|^2\gamma_2}{(\delta_p^2 + \tau_2^{-2})}\right\} \tag{15}$$

where δ_s and δ_p are the signal and pump detunings; the τ's are shown in Fig. 1, the α's, γ's and Δ's are defined in Ref. [1], and $\beta_s = \frac{\vec{\mu}_{32}\vec{E}_s}{2\hbar}$ $\beta_p = \frac{\vec{\mu}_{13} \cdot \vec{E}_p}{2\hbar}$.

To explore the effects of different relaxation rates, we compare the susceptibilities of three different sets of rates at various detunings, pump intensities, and signal intensities. The first set of rates correspond to previous results first obtained by Panock and Temkin[6] in which the decay of each state is uncoupled from the other states and all rates are assumed equal. The next set also assumes equal rates. However, since the rates are the transition rates between level pairs, the pump and signal inversion decays become coupled and the effective decay rates are no longer equal. This set of rates is meant to approximate a homogeneously broadened molecular gas laser in the infrared or far infrared where energy spacings are small compared with the collision energy. In this diabatic collision regime the level pair and polarization decays are collision dominated, and thus, all decay rates are equal to the collision rate.

The third system to be modeled is a cesium vapor Raman laser which is pumped from the $6S_{1/2}$ level to the $8P_{1/2}$ level and emission is to the $8S_{1/2}$ level. The vapor is at low pressure so collisional effects are negligible and decay is dominated by spontaneous emission.

Since the Doppler width of cesium at temperatures above the vaporization temperature is much greater than the homogeneous line width, the susceptibilities must be Doppler integrated to obtain the actual gain of the system. However, it is instructive to first examine the effects of the different relaxation rates on the homogeneous line shape, before including inhomogeneous effects to more accurately predict the tuning curve of a cesium vapor Raman cell as a tunable infrared source. The presence of the $6P_{1/2}$, $7S_{1/2}$ and $7P_{1/2}$ levels complicate matters slightly since the system actually has six levels. However, neglecting the spontaneous emission fields

and assuming the only fields present are the fields nearly resonant with the pump and laser transitions and that all non-resonant contributions of these fields are negligible, then there are no field dependent perturbations connected to the $6S_{1/2}$, $7S_{1/2}$, or $7P_{1/2}$ levels. The energy levels of the cesium system are shown in Fig. 2. The equations of motion of the diagonal elements are as follows:

$$\dot{\rho}_{11} = \frac{-i}{\hbar}(\mu_{31}\rho_{13} - \mu_{13}\rho_{31}) \cdot \vec{E}(t) + t^{-1}_{6p6s}\,\rho_{66} + t^{-1}_{7p6s}\rho_{44} + t^{-1}_{8p6s}\,\rho_{33} \tag{16}$$

$$\dot{\rho}_{22} = \frac{-i}{\hbar}(\mu_{32}\rho_{23} - \mu_{23}\rho_{32}) \cdot \vec{E}(t) + t^{-1}_{8p8s}\,\rho_{33} - \left[t^{-1}_{8s7p} + t^{-1}_{8s6p}\right]\rho_{22} \tag{17}$$

$$\dot{\rho}_{33} = \frac{i}{\hbar}\left[(\mu_{31}\rho_{13} - \mu_{13}\rho_{31}) + (\mu_{23}\rho_{32} - \mu_{32}\rho_{23}\right] \cdot \vec{E}(t) - \left[t^{-1}_{8p8s} + t^{-1}_{8p7s} + t^{-1}_{8p6s}\right]\rho_{33} \tag{18}$$

$$\dot{\rho}_{44} = t^{-1}_{8s7p}\,\rho_{22} - \left[t^{-1}_{7p7s} + t^{-1}_{7p6s}\right]\rho_{44} \tag{19}$$

$$\dot{\rho}_{55} = t^{-1}_{8p7s}\,\rho_{33} + t^{-1}_{7p7s}\rho_{44} - t^{-1}_{7s6p}\,\rho_{55} \tag{20}$$

$$\dot{\rho}_{66} = t^{-1}_{8p6s}\,\rho_{33} + t^{-1}_{7s6p}\rho_{55} + t^{-1}_{6p6s}\,\rho_{66} \tag{21}$$

Where the labels 4, 5, and 6 denote the $7P_{1/2}$, $7S_{1/2}$, and $6P_{1/2}$ labels, respectively, and the zero field equilibrium occupation of the upper levels are negligible. In steady state, Eqs. (16-21) can be rewritten, using $tr\rho = 1$, as two equations in terms of Δ_{13} and Δ_{32} exactly as in the three-level case except the effective rates k_1, k_2, k_3, and k_4 will be different. The dephasing rates in this radiative limit will be taken to be the sum of the spontaneous emission rates of each decay channel for both levels constituting the level pair in question. The dephasing rates are given by

$$\tau_1^{-1} = \tau_{32}^{-1} = t_{8p8s}^{-1} + t_{8p7s}^{-1} + t_{8p6s}^{-1} + t_{8s7p}^{-1} + t_{8s6p}^{-1} \tag{22}$$

$$\tau_2^{-1} = \tau_{31}^{-1} = t_{8p8s}^{-1} + t_{8p7s}^{-1} + t_{8p6s}^{-1} \tag{23}$$

$$\tau_3^{-1} = \tau_{21}^{-1} = t_{8s7p}^{-1} + t_{8s6p}^{-1} \tag{24}$$

The spontaneous emission rates are calculated using

$$\frac{1}{t_{sp}} = \frac{2\ \mu_{ij}^2 \omega^3}{\epsilon h c^3} \tag{25}$$

with the dipole moments obtained from Ref. [13]. The spontaneous emission rates, as well as the effective transverse and longitudinal relaxation rates are given in Table 1.

II. Homogeneous Broadening Results

In this section we compare the imaginary part of the susceptibility at the Raman field frequency, which is responsible for gain or attenuation, for different sets of rates. It will be shown that many of the qualitative features of the previous results, corresponding to the first set of rates, will be changed by the more involved relaxation process occurring in the second two systems. The small signal or unsaturated case was first examined for equal uncoupled decay rates by Javan[2] and later Panock and Temkin[6] as a special case of their work. It was shown that for off resonance pumping ($\delta_p > \Delta\nu$), the susceptibility exhibited two peaks of equal height, one near $\delta_s = 0$ and the other near $\delta_s = \delta_p$, but displaced by the Rabi shift of the energy levels. When the laser field is turned on the symmetry is broken and the $\delta_s \cong 0$ peak saturates faster than the $\delta_s \cong \delta_p$ peak until there is only the peak which shifts towards the center (Fig. 3(a-d)). Physically, this is because the quantum

efficiency of a double quantum transition is one. Or in semiclassical language, it is because the single photon, $\delta_s \cong 0$, contribution is proportional to $\rho_{11} - \rho_{22}$, while the two photon, $\delta_s \cong \delta_p$ is proportional to $\rho_{11} - \rho_{22}$. The effect of the saturating field to first order is to induce transition from ρ_{33} to ρ_{22}, which reduces the single photon inversion, but for any reasonable pump intensities the ground state will have a much greater population than either excited state so that the two photon inversion saturates much slower than the single photon.

When the susceptibility was decomposed into single and double photon contributions, it was seen that the one photon part was absorptive at the gain peak of the two photon part, and similarly, the two photon part was absorptive at the one photon peak. The single photon contribution had a much higher peak than the two photon contribution, but the two photon absorption at the one photon peak was much greater than the one photon absorption at the two photon peak, such that when plotted together the $\delta_s \cong 0$ and the $\delta_s \cong \delta_p$ peaks were of equal height (Fig. 4). It can also be seen from the decomposed susceptibility that the decrease in gain with increasing laser field was due not only to saturation but also to an increasingly more effective competition between gain and absorption. It can be seen in Fig. 5 that initially only the single photon peak saturates until it is approximately equal to the two photon absorption. At this point, the one photon absorption begins to grow while the two photon gain then begins to saturate (Fig. 6).

In addition, the one and two photon contributions nearly cancel, leaving a single peak in the total susceptibility between the original $\delta_s \cong 0$ and $\delta_s \cong \delta_p$ peaks, approximately an order of magnitude less than the peak of the single photon contribution. The absorptive part of the two photon contribution remains approximately the same value as its $\beta_s = 0$ value and only now begins to saturate as both contributions saturate uniformly and the resultant peak in the susceptibility shifts towards $\delta_s = 0$ (Fig. 7).

The on resonance case is harder to interpret in terms of a photon picture, especially at powers at which the Rabi splitting becomes significant. At low pump powers the one and two photon contributions both have peaks at $\delta_s = 0$, with the two photon contribution having absorptive side bands (Fig. 8). At higher powers, the single photon term surprisingly becomes a split absorption peak at $\delta_s = 0$, with gain on the side bands, while the double photon term has a split gain peak with absorption on the side bands (Fig. 9a). The sum of these parts give the familiar Rabi split line shape (Fig. 9b). With increasing signal field both parts saturate and the splitting and sidebands disappear and the one and two photon contributions are respectively single absorption and gain peaks at $\delta_s = 0$. This causes the total susceptibility to decrease in height and the splitting is lost (Fig. 10). The scenario described above applies only to the equal uncoupled rate case.

When the rates are unequal, the resonance behavior is qualitatively similar but there are significant differences in the off resonance behavior. This is to be expected, since the denominators of the population differences Δ_{13} and Δ_{32} contain the population relaxation rates k_1, k_2, k_3, and k_4 , as well as τ_1, τ_2, and τ_3 in the different parts, which alter what might be called the effective saturation intensities of the different parts. Even for $\beta_s = 0$ there will be differences because of a bottlenecking effect which occurs when one of the population relaxation rates is less than the others and thus cannot relax fast enough to keep the occupation of that level down to the valve it would have in the equal rate case. As a result the balance of absorption and gain required to make the $\delta_s \cong 0$ and the $\delta_s \cong \delta_p$ peaks equal at $\beta_s = 0$ will not be present.

In the FIR system with coupled rates, the gain of the one photon term is less than the absorption of the two photon term, and therefore, the resulting susceptibility has net absorption not gain at $\delta_s \cong 0$ (Fig. 11). Then, as the signal field is turned on, the peak of the one photon term increases to cancel the two

photon absorption instead of saturating, as would be expected (Fig. 12).

In the cesium system the peak of the two photon term is much greater than the one photon peak or the two photon absorption, which makes the $\delta_s \cong \delta_p$ peak in the susceptibility about an order of magnitude larger than the $\delta_s \cong 0$ (Fig. 13) peak. For increasing values of β_s, the two photon peak saturates very rapidly, since the single photon peak is approximately the same height as the two photon absorption. The one photon term also has a small gain peak as well as an absorption peak at the two photon gain peak (Fig. 14).

Another difference between the cesium system and the previous two is the narrowness of the two photon gain peak. This is because in the cesium set of rates the polarization decay rates are due to spontaneous emission and not collisions. Since all of the rates in the plots are normalized to τ_1 and the width is roughly determined by τ_1/τ_3, which is the relative rate of two-photon coherence decay. In the first two systems this number is unity, while in the cesium system it is $\tau_1/\tau_3 = 0.063$. Fig. 15(a) shows how the $\delta_s \cong \delta_p$ peak narrows as the two photon contribution becomes more dominant with increasing pump field detuning, while Figs. 15(b), (c) shows how the width of the the peaks in the other two rate cases remains about the same.

Figs. 15(a-c) also show that the absolute maximum of the susceptibility initially increases with pump detuning at constant pump field in both the cesium and the coupled rate FIR system, while there is a monotonic decrease in the equal rate case. Figs. 16-18 show the value of the absolute maximum of the susceptibilities as a function of increasing pump detuning for pump field Rabi frequencies of two, five, and ten in units of τ_1^{-1}. In the equal rate case there is always a rapid monotonic decrease, and although the coupled rate FIR system rises to a peak, it then decreases rapidly with detuning. The cesium system has its maximum gain at a greater detuning than the FIR system and falls off much slower with detuning. This

suggests that the cesium may be used more effectively as a tunable laser medium than would be expected from looking at the equal rate case, since there is an appreciable gain peak over a significantly larger range of detunings.

Fig. 19 shows the position of the peak signal frequency detuning as a function of pump detuning and the deviation from $\delta_s = \delta_p$ as $\delta_s - \delta_p$ is plotted vs. β_p. The peak location is the same for the three sets of rates, illustrating that for this range of pump power, the peak location depends only on β_p and δ_p. At $\delta_p = 0$ the peak is located at $\delta_s = \beta_p$, the Rabi frequency. Only at very low powers where the Rabi splitting is not simply equal to the Rabi frequency do the rates affect the position of the peaks (Fig. 20). Fig. 21 shows the peak position vs. pump field Rabi frequency β_p at $\delta_p = 0$ and $\delta_p = 10$. For $\delta_p = 0$, the peak is at $\delta_s = 0$ for low power, then splits at different powers for the three different rate cases, and eventually approaches $\delta_s = \beta_p$ at higher powers. For $\delta_p = 10$, the peak is at $\delta_s = \delta_p$ and then as pump power is increased the peak shifts towards $\delta_s = \beta_p$.

III. Inhomogeneous Model

In this section we will examine the effects of Doppler broadening in the cesium system for different values of the pump field detunings and Rabi frequencies. We will first see how the gain curves evolve as the detuning approaches and exceeds the Doppler width. Then, in the second half of this section, we will compare the predicted tuning curves for the Doppler broadened system vs. the homogeneous system for pump detunings and pump Rabi frequencies much greater than the Doppler width, as would be present in the doubled alexandrite pumped cesium vapor Raman laser.

The Doppler broadened gain is given by the homogeneous response of a specific velocity group integrated over the Boltzman velocity distribution, which can be written as

$$\chi_{Dop} = \sqrt{\frac{\ln 2}{\pi}} \frac{2}{\Delta\omega_{Dop}} \int_{-\infty}^{\infty} \chi_h(\delta_s \mp \epsilon\,\omega,\ \delta_p - \omega) e^{-4\ln 2(\omega/\Delta\omega_{Dop})^2} d\omega \qquad (26)$$

where $\epsilon = k_s/k_p$, k_p and k_s are, respectively, the pump and signal field wave vectors, ω is the angular frequency shift of the pump, and $\Delta\omega_{Dop}$ is the full width at half max of the pump transition given by

$$\Delta\omega_{Dop} = 2k_p \sqrt{\frac{2kT\ln 2}{M}} \quad . \qquad (27)$$

The - and + are, respectively, the co- and counter-propagating beams.

For cesium, the transition energies in wave numbers are 25709 cm^{-1} for the $6S_{1/2}8P_{1/2}$ transition and 1572 cm^{-1} for the $8S_{1/2}8P_{1/2}$ transition. Using these values and a temperature of 1000K[14] (the cesium vaporization temperature is 932K), $\Delta\omega_{Dop}$

and the wave vector ratio were calculated to be

$$\Delta\omega_{Dop} = 54.5\ \tau_1^{-1} \quad \epsilon = k_s/k_p = 0.061 \tag{28}$$

The integral was evaluated numerically.

For small pump field and detunings[7] within the Doppler width, the line shape exhibits a co- and counter-propagating asymmetry with the co-propagating peak located at $\epsilon\delta_p$ and the counter-propagating peak located at $-\epsilon\delta_p$. The co-propagating peak is slightly higher and narrower than the counter-propagating peak by approximately $1 + \epsilon$ (Fig. 22), and as the pump Rabi frequency is increased above $\beta_p \simeq 7/5\ \tau_1^{-1}$, the co-propagating peak splits, although the magnitude of the splitting is less than in the homogeneous case (Fig. 23).

As the detuning is increased, the co-propagating split disappears, and a wide peak begins to appear at the Rabi shifted two photon resonance. The origin of this can be seen by approximating the homogeneous line as a sum of delta function responses at the one and two photon resonances.

$$\chi_h = V_1\,\delta(\delta_s - \Delta_s) + V_2\,\delta(\delta_s - \delta_p - \Delta_2) \tag{29}$$

where V_1 and V_2 are the areas of the two peaks, and Δ_1 and Δ_2 are the Rabi light shifts. Although the homogeneous line will only look like delta functions when $(k_s/k_p)\ \Delta\omega_{Dop} >> \tau_i,\ k_i$, this approximation shows some important features of the fully integrated line shape.

$$\chi_{Dop} \propto \frac{V_1}{\epsilon\Delta\omega_{Dop}}\, e^{-4\ln 2\left[\frac{\delta_s - \Delta_1}{\epsilon\Delta\omega_{Dop}}\right]^2} + \frac{V_2}{(1\mp\epsilon)\Delta\omega_{Dop}}\, e^{-4\ln 2\left[\frac{\delta_s - \delta_p - \Delta_2}{(1\mp\epsilon)\,\Delta\omega_{Dop}}\right]^2} \tag{30}$$

where the weak dependence of Δ_1 and Δ_2 on δ_p was neglected. The first term is just a gaussian near line center with the width of the laser transition $\epsilon\Delta\omega_{Dop}$. The second term near $\delta_s \simeq \delta_p$ is what the Raman peak becomes in the presence of Doppler broadening. It is a gaussian with the width of the pump transition $\mp$ the width of the laser transition, depending on co- or counter-propagating beams. Also, the peak value of the homogeneous two photon transition is diminished by $1/(1\mp\epsilon)\Delta\omega_{Dop}$, while the one photon peak is only diminished by $1/\epsilon\Delta\omega_{Dop}$. Thus, the $\delta_s = \Delta_1$ peak will be higher and narrower than the $\delta_s = \delta_p + \Delta_2$ peak. Fig. 24 shows the fully integrated co- and counter-propagating gain curve for $\delta_p = 200\tau_1^{-1}$ and $\beta_p = \tau_1^{-1}$. It is interesting to contrast the Doppler integrated gain where the one photon peak is significantly higher than the two photon peak, with the homogeneous gain curve, in which the single photon peak is almost negligible in comparison to the two photon peak (Fig. 25).

For higher pump powers the on resonance counter-propagating gain peak begins to split (Fig. 26), and as the pump Rabi frequency, β_p, approaches the half width of the Doppler distribution, both the co- and counter-propagating gain curves split into two distinct peaks located at $\pm\beta_p$. The evolution of the curves with increasing detuning proceeds much the same as the low pump power except that the co- and counter-propagating asymmetry persists on the single photon peak.

We will now compare the predicted gain tuning curves of a doubled alexandrite pumped cesium vapor Raman laser to examine the effects of Doppler broadening. The alexandrite laser is a solid state laser, tunable from 7000Å to 8000Å. We will assume a pulsed laser with an energy of 150 mJ/pulse and a pulse width of τ = 300 ns, focused to a spot size of 100 μm radius, which gives a peak Rabi frequency of $\beta_p \cong 3.6 \times 10^5\tau_1^{-1}$. The tuning range which will be examined is from 25709 cm^{-1} to 27200 cm^{-1}, keeping in mind that the higher wave numbers will begin to pump the $9P_{1/2}$ level, and thus will be most accurate closer to resonance. When

tuned to resonance at peak power, the susceptibility has two peaks Rabi split to approximately ±275 cm^{-1} wave number detuning from the laser transition line center. The peak position is the same for both the homogeneous and inhomogeneous susceptibilities, although the peak gain value is much lower in the Doppler case than it would be if the system were not inhomogeneously broadened. As the pump is detuned the peak closest to the pump frequency begins to increase and move away from the center, while the other peak decreases and moves towards line center. Fig. 27 shows the resonantly pumped susceptibility and the value of the peak as the detuning is increased. In Fig. 28 the position of the peak is given for varying pump detunings, with the diagonal line denoting the $\delta_s = \delta_p$ line. The dotted line indicates the peak closer to line center, while the solid line indicates the "two photon" peak, which approaches $\delta_s = \delta_p$ as the detuning becomes large compared with the Rabi frequency.

When inhomogeneous broadening is taken into account, there is a drastic deviation from the homogeneous results. Although the peak position remains the same as in the homogeneous line, the peak which approaches $\delta_s = \delta_p$, widens and decreases in height from its $\delta_p = 0$ value while the other peak narrows and increases sharply, even though the detuning and Rabi frequency are both huge in comparison to the Doppler width. Figure 29 shows how the peak changes with detuning from the $\delta_p = 0$ value.

This illustrates the necessity of including Doppler broadening in the gain calculation for such a system. The essence of the lower gain on the two photon transition is because of the near proportionality of peak position, δ_s, to pump detuning, δ_p. In contrast to the homogeneous calculations, including the calculation of $\chi^{(3)}$ [9,10,11] in which each atom radiates at the same frequency, the Doppler broadened calculation includes a frequency shifted peak for each velocity group. This results in a two photon gain which is spread out with the width approximately equal

to the Doppler width of the pump transition and height proportionately diminished, as shown in Eq. (30). In addition, if the vapor cell is used as a one or two pass Raman amplifier, the line width of the output radiation will be that of the pump Doppler width, and not the homogeneous or power broadened linewidth.

IV. Conclusion

We have examined the imaginary susceptibility on the laser transition (proportional to the gain or attenuation) of a three-level system, with arbitrary relaxation rates, detunings, and field strengths interacting with two laser fields, obtained analytically in the density matrix formalism. The solution assumed negligible spatial and temporal variation and monochromatic laser fields (laser line width much smaller than the homogeneous width). It was found that differing relaxation rates cause important qualitative differences, and some case, gain in one system may become absorption in another.

The results were then applied to a cesium vapor laser pumped by a tunable pulsed doubled alexandrite laser. Since the pulse width is just slightly larger than the homogeneous line width, the system will be just on the limit of the adiabatic following regime. Therefore, the steady state results can only be loosely applied and must serve as a rough model for the position and relative strengths of the gain peaks. Another complication due to the pulsed pump arose because of the sensitivity of the gain peak position on pump field strength. This will result in "chirped" output pulses. However, since the peak gain for fixed detuning and pulsed pump field strength occurs at the peak of the pump pulse, the dominant contribution to the output gain will come from the peak field strength, resulting in a relatively narrow output pulse.

The system was then Doppler integrated, since the Doppler width is many times the homogeneous width. It was found that even though the detuning and Rabi frequency were much greater than the Doppler width, it caused the gain to shift from the predominantly two photon ($\delta_s \simeq \delta_p$) homogeneous susceptibility result to a predominantly single photon contribution ($\delta_s \sim 0$).

Acknowledgment

The authors are grateful to Dr. J. J. Degnan of the Goddard Space Flight Center for his useful discussions concerning the directions of this work. We are also grateful to Mr. Jan Nordgren for his help with the numerical analysis.

References

[1] J. C. Ryan and N. M. Lawandy, "Density Matrix Solutions for the Susceptibilities of a Three-Level System with Arbitrary Relaxation Rates and Field Strengths," IEEE JQE, Vol. QE22(11), 2075-2078, 1986.

[2] A. Javan, "Theory of a Three Level Maser," Phys. Rev., Vol. 107, pp. 1579-1589, 1957.

[3] A. M. Clogston, "Susceptibility of the Three Level Maser," J. Phys. Chem. Solids, Vol. 4, pp. 271-277, 1958.

[4] S. Yatsiv, "Role of Double Quantum Transitions in Masers," Phys. Rev., Vol. 113, pp. 1538-1544, 1959.

[5] R. G. Brewer and E. L. Hahn, "Coherent Two Photon Processes: Transient and Steady State Cases," Phys. Rev. A, Vol. II, pp. 1641-1649, 1975.

[6] R. L. Panock and R. J. Temkin, "Interaction of Two Laser Fields with a Three Level Molecular System," IEEE JQE, Vol. QE-13, pp. 425-434, 1977.

[7] M. S. Feld and A. Javan, "Laser-Induced Line-Narrowing Effects in Coupled Doppler Broadened Transitions," Phys. Rev., Vol. 177, pp. 540-562, 1969.

[8] D. Seligson, Martial Ducay, J. R. R. Leite, A. Sanchez, and M. S. Feld, "Quantum Mechanical Features of Optically Pumped CW FIR Lasers," IEEE JQE, Vol. QE-13, pp. 468-472, 1977.

[9] J. J. Wynne and P. P. Sorokin, "Optical Mixing in Atomic Vapors," in Nonlinear Infrared Generation, Y.-R. Shen, Ed., Berlin-Heidelberg: Springer-Verlag, 1977.

[10] D. Cotter, D. C. Hanna, P. A. Kärkkäinen, R. Wyatt, "Stimulated Electronic Raman Scattering as a Tunable Infrared Source," Opt. Commun., Vol. 15, pp. 143-146, October 1975.

[11] D. Cotter, D. C. Hanna, "Stimulated Electronic Raman Scattering in Cs Vapor: A Simple Tunable Laser System for the 2.7 to 3.5 μm Region," Optical and Quantum Electronics, Vol. 9, pp. 509-518, 1977.

[12] N. M. Lawandy, Ali Fahmy, and Kayee Lee, "Excitation Dependent Dephasing and the Stability of the Lorenz Model for a Homogeneously Broadened Unidirectional Ring Laser," International Meeting on Instabilities and Dynamics of Lasers and Nonlinear Optical Systems," Rochester, NY, 1985.

[13] Richard B. Miles and Stephen E. Harris, "Optical Third Harmonic Generation in Alkali Metal Vapors," IEEE JQE, Vol. QE9, pp. 470-484, 1973.

[14] C. R. Vidal and J. Cooper, "Heat Pipe Oven for Spectroscopic Measurements," J. Appl. Phys., Vol. 40, pp. 3370-3374, 1969.

Figure Captions

Figure 1: Schematic of 3-level system.

Figure 2: Energy levels of atomic cesium.

Figure 3: $\chi_s'' \hbar/\tau_1\mu^2\epsilon_o$ is plotted versus $\delta_s\tau_1$ with decreasing amplitude corresponding to increasing stimulated fields of $\beta_s\tau_1 = 0, 1, 2, 5$ and (a) $\beta_p\tau_1 = 1$, $\delta_p\tau_1 = 5$, (b) $\beta_p\tau_1 = 5$, $\delta_p\tau_1 = 5$, (c) $\beta_p\tau_1 = 1$, $\delta_p\tau_1 = 10$, (d) $\beta_p\tau_1 = 5$, $\delta_p\tau_1 = 10$.

Figure 4: (a) One and two photon terms with two photon term absorption near $\delta_s\tau_1 = 0$ of $\chi_s'' \hbar/\tau_1\mu^2\epsilon_o$ and (b) $\chi_s'' \hbar/\tau_1\mu^2\epsilon_o$ are plotted versus $\delta_s\tau_1$ for $\delta_p\tau_1 = 10$, $\beta_p\tau_1 = 2$, $\beta_s\tau_1 = 0$.

Figure 5: Same as Fig. 4 except for $\delta_p\tau_1 = 10$, $\beta_p\tau_1 = 2$, $\beta_s\tau_1 = 1$.

Figure 6: Same as Fig. 4 except for $\delta_p\tau_1 = 10$, $\beta_p\tau_1 = 2$, $\beta_s\tau_1 = 5$.

Figure 7: Same as Fig. 4 except for $\delta_p\tau_1 = 10$, $\beta_p\tau_1 = 2$, $\beta_s\tau_1 = 10$.

Figure 8: (a) One photon term has higher amplitude of $\chi_s'' \hbar/\tau_1\mu^2\epsilon_o$ and (b) $\chi_s'' \hbar/\tau_1\mu^2\epsilon_o$ are plotted versus $\delta_s\tau_1$ for $\delta_p\tau_1 = 0$, $\beta_p\tau_1 = 0.2$, $\beta_s\tau_1 = 0$.

Figure 9: (a) Single photon term is absorptive at $\delta_s = 0$ and (b) $\chi_s'' \hbar/\tau_1\mu^2\epsilon_o$ are plotted versus $\delta_s\tau_1$ for $\delta_p\tau_1 = 0$, $\beta_p\tau_1 = 5$, $\beta_s\tau_1 = 0$.

Figure 10: Same as Fig. 9 except for $\delta_p\tau_1 = 0$, $\beta_p\tau_1 = 5$, $\beta_s\tau_1 = 8$.

Figure 11: Same as Fig. 4 except with coupled FIR rates for $\delta_p\tau_1 = 10$, $\beta_p\tau_1 = 2$, $\beta_s\tau_1 = 0$.

Figure 12: Same as Fig. 11 except for $\delta_p\tau_1 = 10$, $\beta_p\tau_1 = 2$, $\beta_s\tau_1 = 2$.

Figure 13: Same as Fig. 11 except with cesium rates for $\delta_p\tau_1 = 10$, $\beta_p\tau_1 = 2$, $\beta_s\tau_1 = 0$.

Figure 14: Same as Fig. 13 except for $\delta_p\tau_1 = 10$, $\beta_p\tau_1 = 2$, $\beta_s\tau_1 = 1$.

Figure 15: $\chi_s'' \hbar/\tau_1\mu^2\epsilon_o$ is plotted versus $\delta_s\tau_1$ at values of $\delta_p\tau_1 = 2, 7, 10, 15$ for (a) cesium rates and (b) equal coupled rates.

Figure 16: Peak value of $\chi_s'' \hbar/\tau_1\mu^2\epsilon_o$ is plotted versus $\delta_s\tau_1$ at $\beta_p\tau_1 = 2$, $\beta_s\tau_1 = 0$ for (a) cesium rates, (b) equal coupled FIR rates, and (c) equal uncoupled rates.

Figure 17: Peak value of $\chi_s'' \hbar/\tau_1\mu^2\epsilon_o$ is plotted versus $\delta_p\tau_1$ at $\beta_p\tau_1 = 5$, $\beta_s\tau_1 = 0$ for (a) cesium rates, (b) equal coupled FIR rates, and (c) equal uncoupled rates.

Figure 18: Peak value of $\chi_s'' \hbar/\tau_1\mu^2\epsilon_o$ is plotted versus $\delta_p\tau_1$ at $\beta_p\tau_1 = 10$, $\beta_s\tau_1 = 0$ for (a) cesium rates, (b) equal coupled FIR rates, and (c) equal uncoupled rates.

Figure 19: (a) peak position ($\delta_s\tau_1$) peak is plotted versus $\delta_p\tau_1$ at $\beta_p\tau_1 = 10$, $\beta_s\tau_1 = 0$ and (b) deviation from $\delta_s = \delta_p$ is plotted versus $\delta_p\tau_1$.

Figure 20: (a) peak position ($\delta_s\tau_1$) peak is plotted versus $\beta_p\tau_1$ at $\delta_p\tau_1 = 0$, $\beta_s\tau_1 = 0$ for (a) cesium rates, (b) equal coupled FIR rates, and (c), equal uncoupled rates.

Figure 21: (a) peak position ($\delta_s\tau_1$) peak is plotted versus $\beta_p\tau_1$ at $\delta_p\tau_1 = 10$, $\beta_s\tau_1 = 0$.

Figure 22: (a) Co-propagating and (b) counter-propagating values of $\chi_s'' \hbar/\tau_1\mu^2\epsilon_o$ versus $\delta_s\tau_1$ Doppler integrated at $\beta_p\tau_1 = 0.5$, $\beta_s\tau_1 = 0$, $\delta_p\tau_1 = 10$.

Figure 23: (a) Co-propagating and (b) counter-propagating values of $\chi_s'' \hbar/\tau_1\mu^2\epsilon_o$ versus $\delta_s\tau_1$ Doppler integrated at $\beta_p\tau_1 = 1.0$, $\beta_s\tau_1 = 0$, $\delta_p\tau_1 = 10$.

Figure 24: (a) Co-propagating and (b) counter-propagating values of $\chi_s'' \hbar/\tau_1\mu^2\epsilon_o$ versus $\delta_s\tau_1$ Doppler integrated at $\beta_p = 1.0$, $\beta_s\tau_1 = 0$, $\delta_p\tau_1 = 200$.

Figure 25: Homogeneous value of $\chi_s'' \hbar/\tau_1\mu^2\epsilon_o$ versus $\delta_s\tau_1$ for $\beta_p = 1.0$, $\beta_s = 0$, $\delta_p\tau_1 = 200$.

Figure 26: (a) Co-propagating and (b) counter-propagating $\chi_s'' \hbar/\tau_1\mu^2\epsilon_o$ versus $\delta_s\tau_1$ Doppler integrated at $\beta_p\tau_1 = 20$, $\beta_s\tau_1 = 0$, $\delta_p\tau_1 = 0$.

Figure 27: Vertical lines are a plot of the on resonant $\chi_s'' \hbar/\tau_1\mu^2\epsilon_o$ at $\beta_s = 3.6 \times 10^5\tau_1$, and the curves are a plot of the maximum value of the respective homogeneous peaks versus δ_s in wave numbers as pump detuning is decreased below zero.

Figure 28: A plot of the values of the two peaks of $\chi_s'' \hbar/\tau_1\mu^2\epsilon_o$ at $\beta_s = 3.6 \times 10^5\tau_1$ versus δ_p in wave numbers.

Figure 29: Vertical lines are a plot of the on resonant Doppler integrated $\chi_s'' \hbar/\tau_1\mu^2\epsilon_o$ at $\beta_s = 3.6 \times 10^5\tau_1$, and the curves are a plot of the maximum value of the respective Doppler integrated peaks versus δ_s in wave numbers as pump detuning is decreased below zero.

Table 1

Transition	Dipole Matrix Element (C-m)	Spontaneous Lifetime (Sec)
$6s_{1/2}6p_{1/2}$	2.8×10^{-29}	1.09×10^{-8}
$6s_{1/2}7p_{1/2}$	3.1×10^{-30}	1.17×10^{-7}
$6s_{1/2}8p_{1/2}$	1.4×10^{-30}	3.59×10^{-7}
$6p_{1/2}7s_{1/2}$	2.6×10^{-29}	4.54×10^{-8}
$6p_{1/2}8s_{1/2}$	5.7×10^{-30}	1.68×10^{-7}
$7s_{1/2}7p_{1/2}$	6.1×10^{-29}	9.41×10^{-8}
$7s_{1/2}8p_{1/2}$	6.6×10^{-29}	7.30×10^{-9}
$6p_{1/2}8s_{1/2}$	5.8×10^{-29}	2.67×10^{-7}
$8s_{1/2}8p_{1/2}$	1.0×10^{-28}	2.77×10^{-7}

Effective Rates (sec^{-1})

$k_1 = 2.62 \times 10^7$	$\tau_1^{-1} = 1.53 \times 10^8$
$k_2 = 3.06 \times 10^7$	$\tau_2^{-1} = 1.43 \times 10^8$
$k_3 = 1.24 \times 10^7$	$\tau_3^{-1} = 9.71 \times 10^6$
$k_4 = 2.60 \times 10^7$	

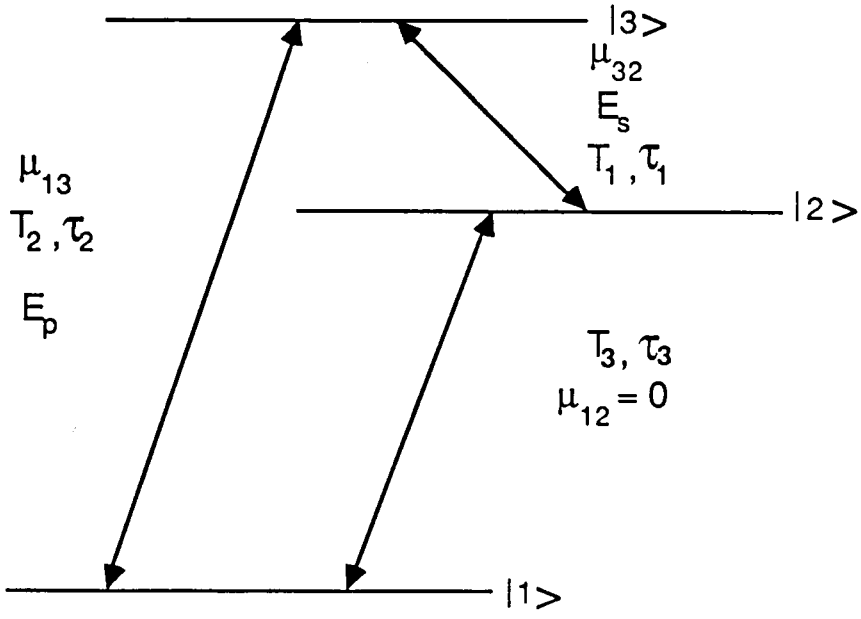

Fig. 1

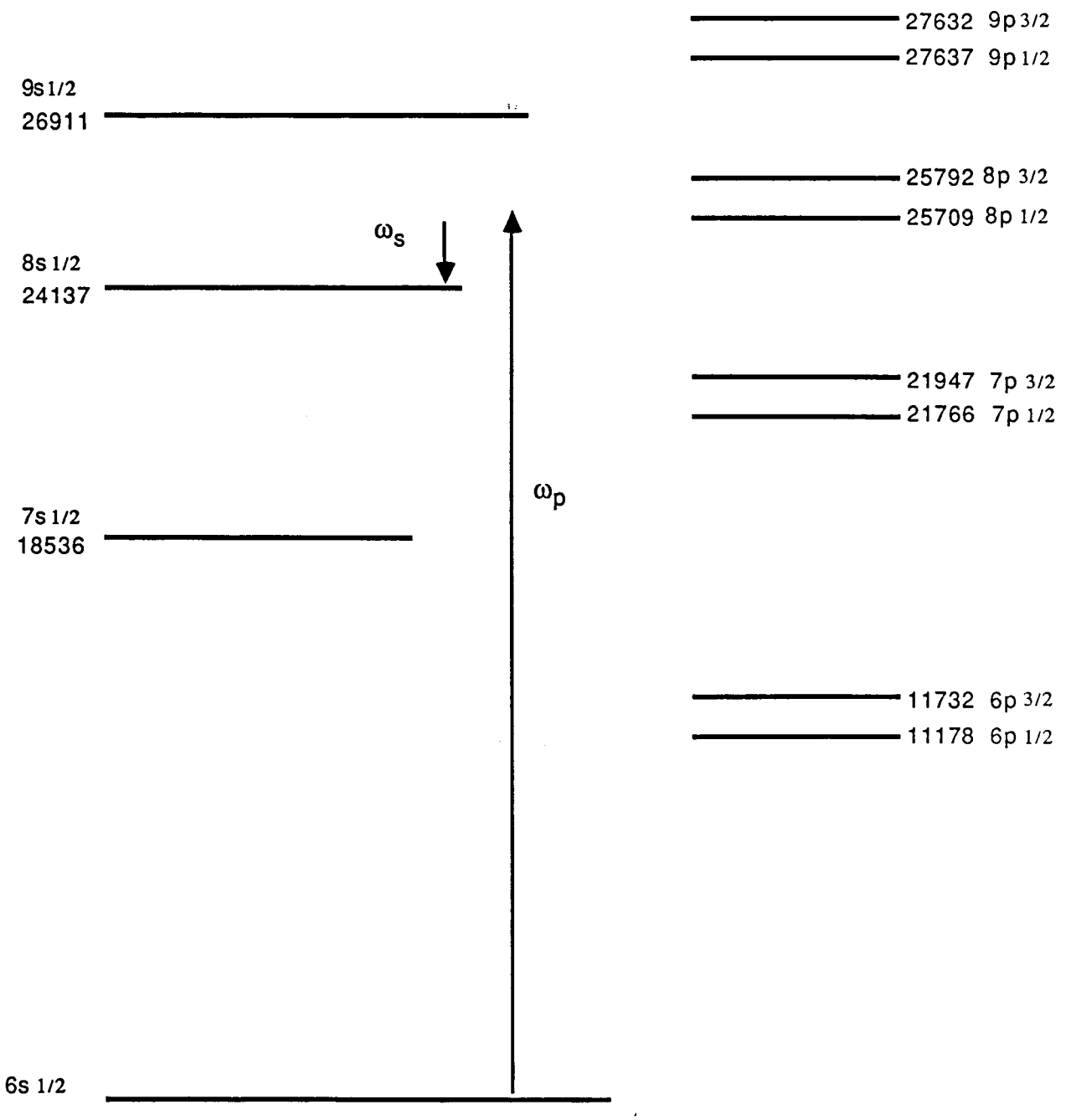
27632 9p 3/2
27637 9p 1/2
9s 1/2
26911
25792 8p 3/2
25709 8p 1/2
ω_s
8s 1/2
24137
21947 7p 3/2
21766 7p 1/2
ω_p
7s 1/2
18536
11732 6p 3/2
11178 6p 1/2
6s 1/2

Fig. 2

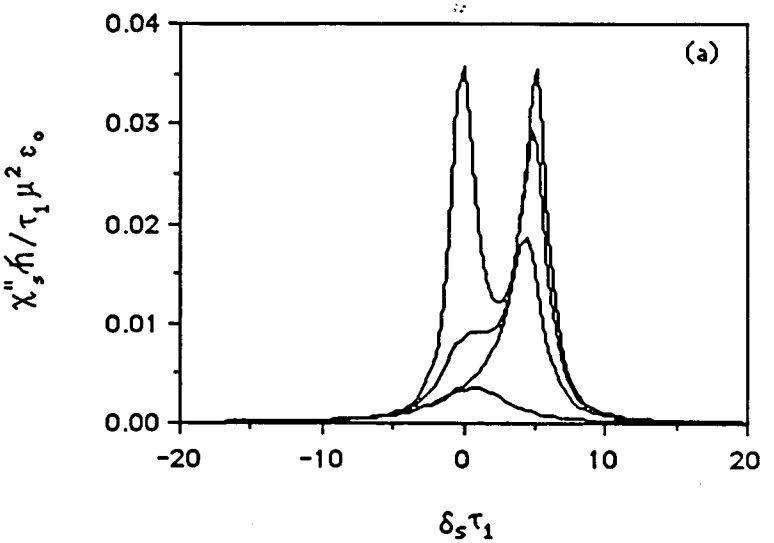
(a)
0.04
0.03
0.02
0.01
0.00
-20
-10
0
10
20
$\chi''_s\hbar/\tau_1\mu^2\varepsilon_o$
$\delta_s\tau_1$

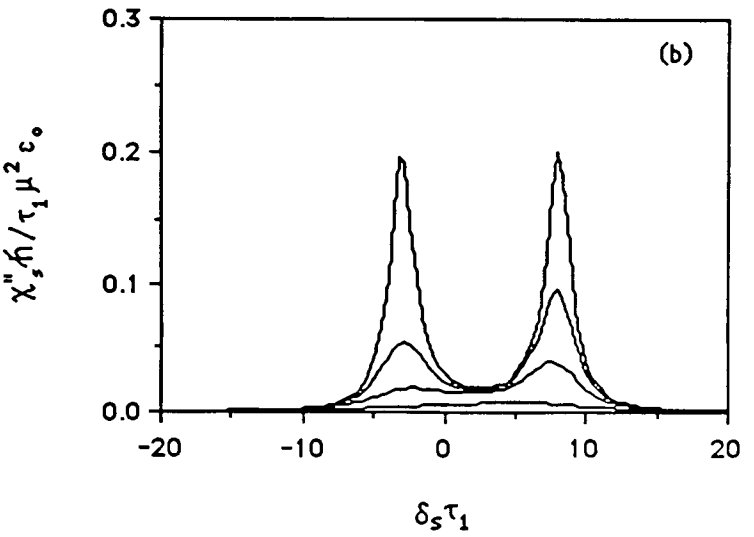
(b)
0.3
0.2
0.1
0.0
-20
-10
0
10
20
$\chi''_s\hbar/\tau_1\mu^2\varepsilon_o$
$\delta_s\tau_1$

Fig. 3

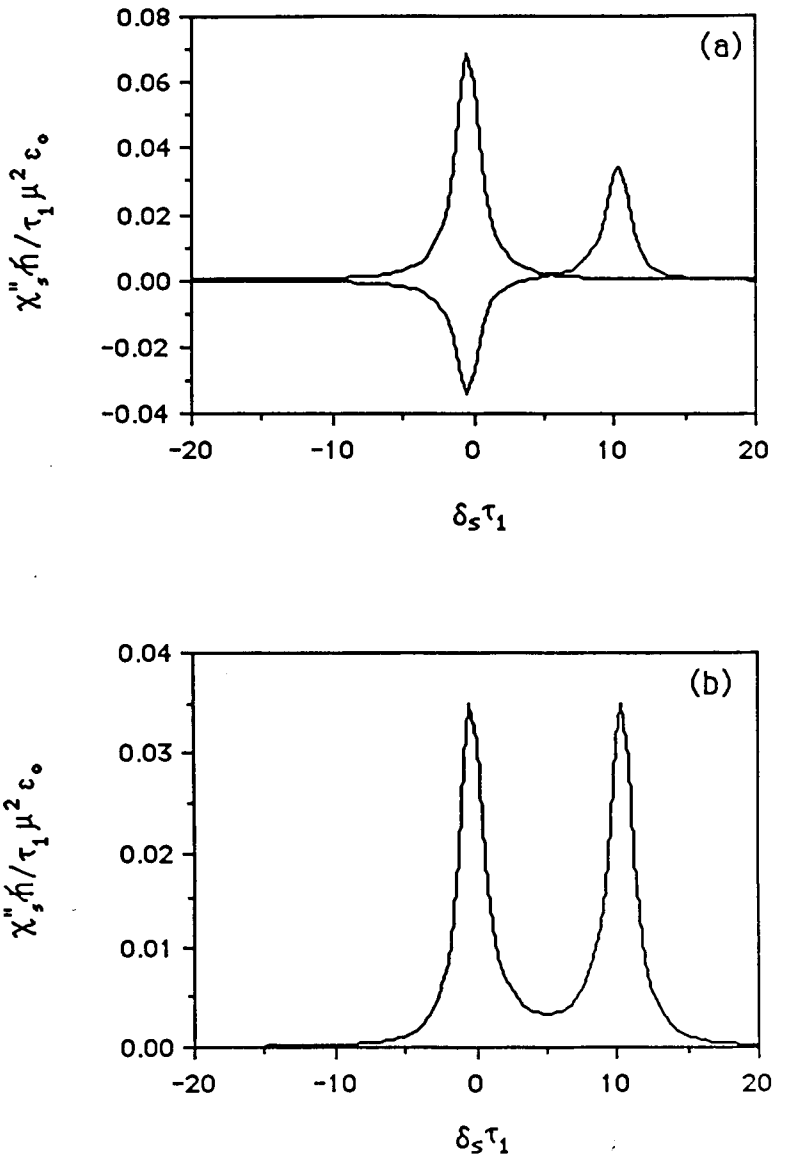
(a)
0.08
0.06
0.04
0.02
0.00
-0.02
-0.04
-20
-10
0
10
20
$\chi''_s\hbar/\tau_1\mu^2\varepsilon_o$
$\delta_s\tau_1$
(b)
0.04
0.03
0.02
0.01
0.00
-20
-10
0
10
20
$\chi''_s\hbar/\tau_1\mu^2\varepsilon_o$
$\delta_s\tau_1$

Fig. 4

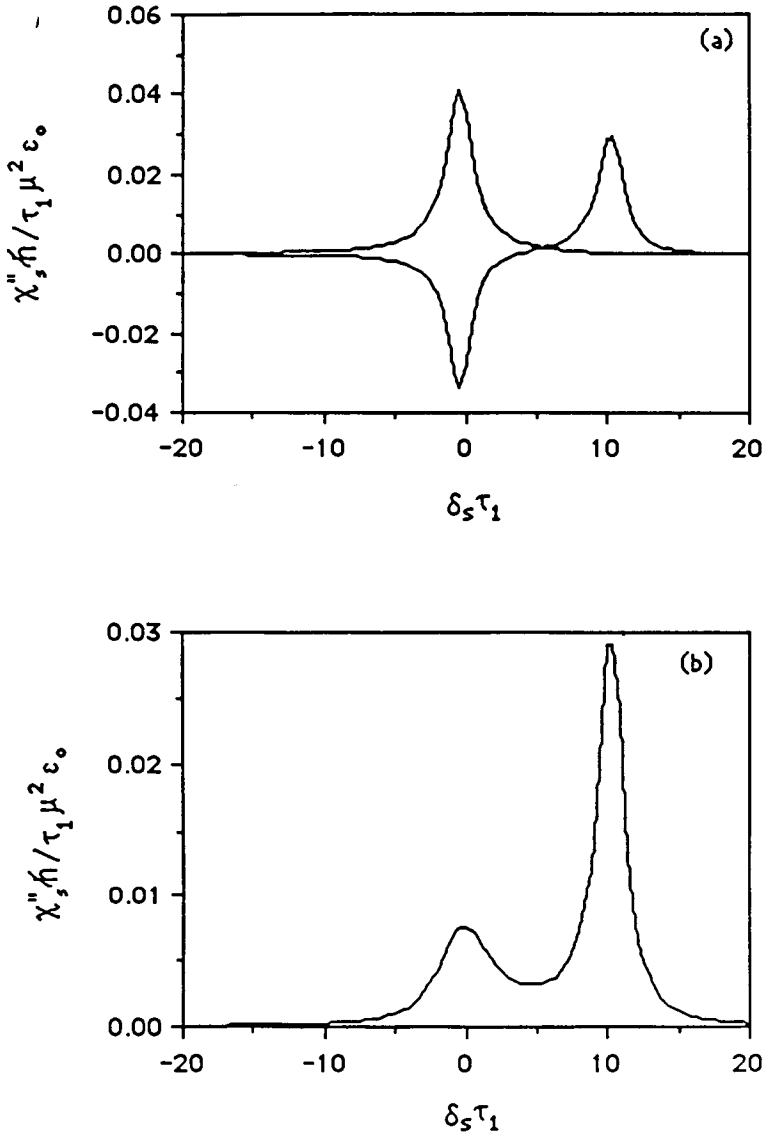
(a)
0.06
0.04
0.02
0.00
-0.02
-0.04
-20
-10
0
10
20
$\chi''_s\hbar/\tau_1\mu^2\varepsilon_o$
$\delta_s\tau_1$
(b)
0.03
0.02
0.01
0.00
-20
-10
0
10
20
$\chi''_s\hbar/\tau_1\mu^2\varepsilon_o$
$\delta_s\tau_1$

Fig. 5

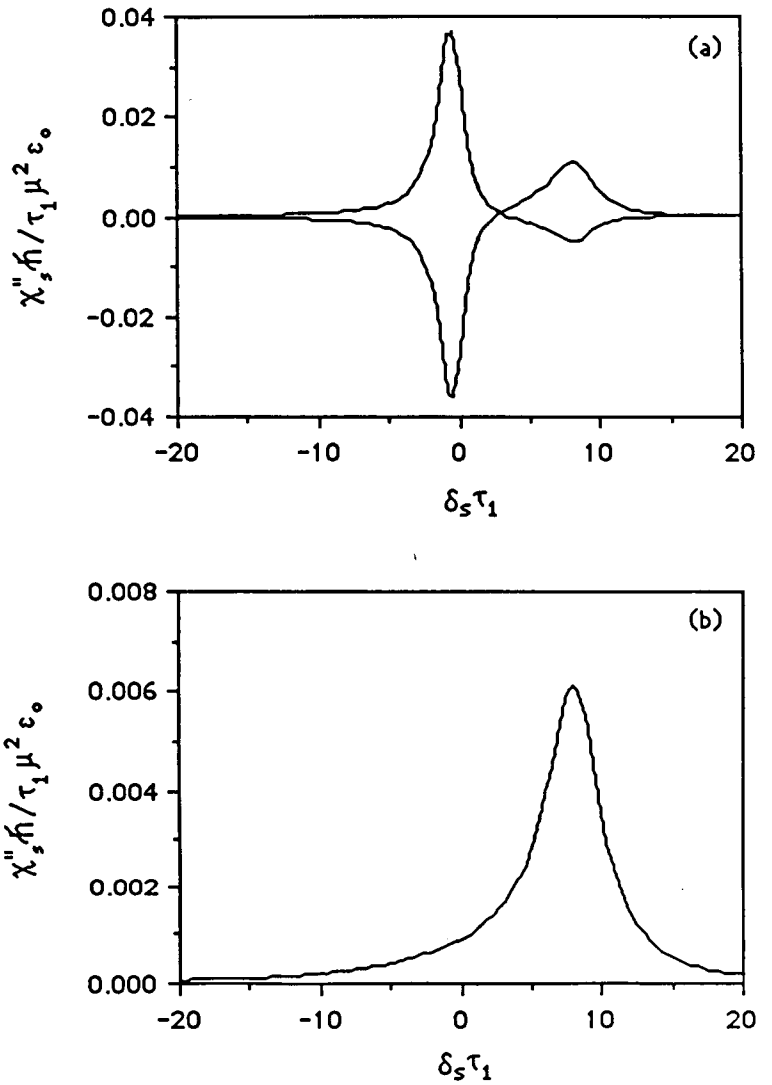
0.04
0.02
0.00
-0.02
-0.04
(a)
$\chi''_s\hbar/\tau_1\mu^2\varepsilon_o$
-20
-10
0
10
20
$\delta_s\tau_1$
0.008
0.006
0.004
0.002
0.000
(b)
$\chi''_s\hbar/\tau_1\mu^2\varepsilon_o$
-20
-10
0
10
20
$\delta_s\tau_1$

Fig. 6

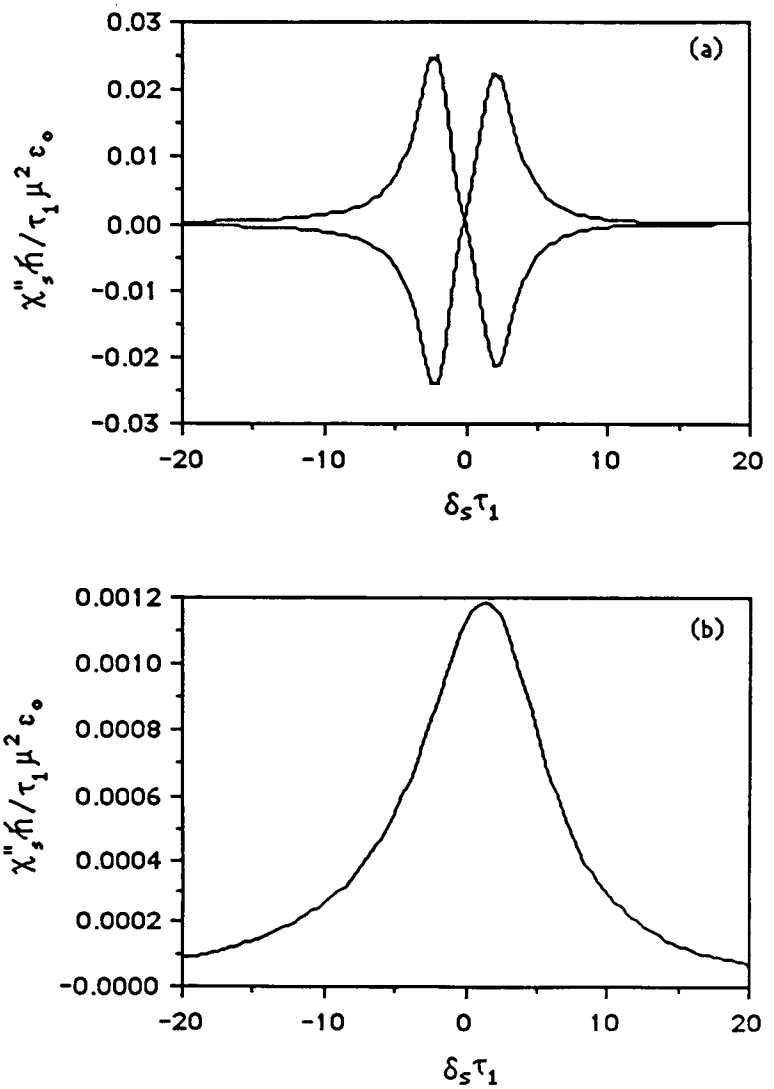
(a)
0.03
0.02
0.01
0.00
-0.01
-0.02
-0.03
-20
-10
0
10
20
$\chi''_s\hbar/\tau_1\mu^2\varepsilon_o$
$\delta_s\tau_1$
(b)
0.0012
0.0010
0.0008
0.0006
0.0004
0.0002
-0.0000
-20
-10
0
10
20
$\chi''_s\hbar/\tau_1\mu^2\varepsilon_o$
$\delta_s\tau_1$

Fig. 7

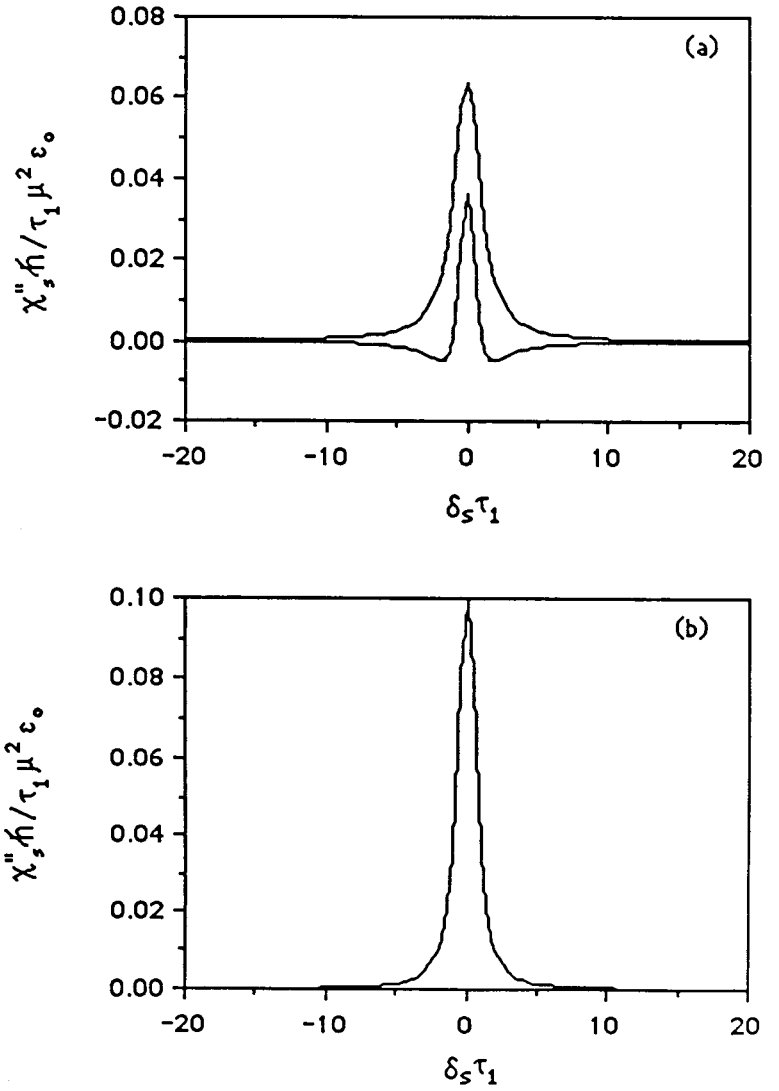
(a)
0.08
0.06
0.04
0.02
0.00
-0.02
-20
-10
0
10
20
$\chi''_s\hbar/\tau_1\mu^2\varepsilon_o$
$\delta_s\tau_1$
(b)
0.10
0.08
0.06
0.04
0.02
0.00
-20
-10
0
10
20
$\chi''_s\hbar/\tau_1\mu^2\varepsilon_o$
$\delta_s\tau_1$

Fig. 8

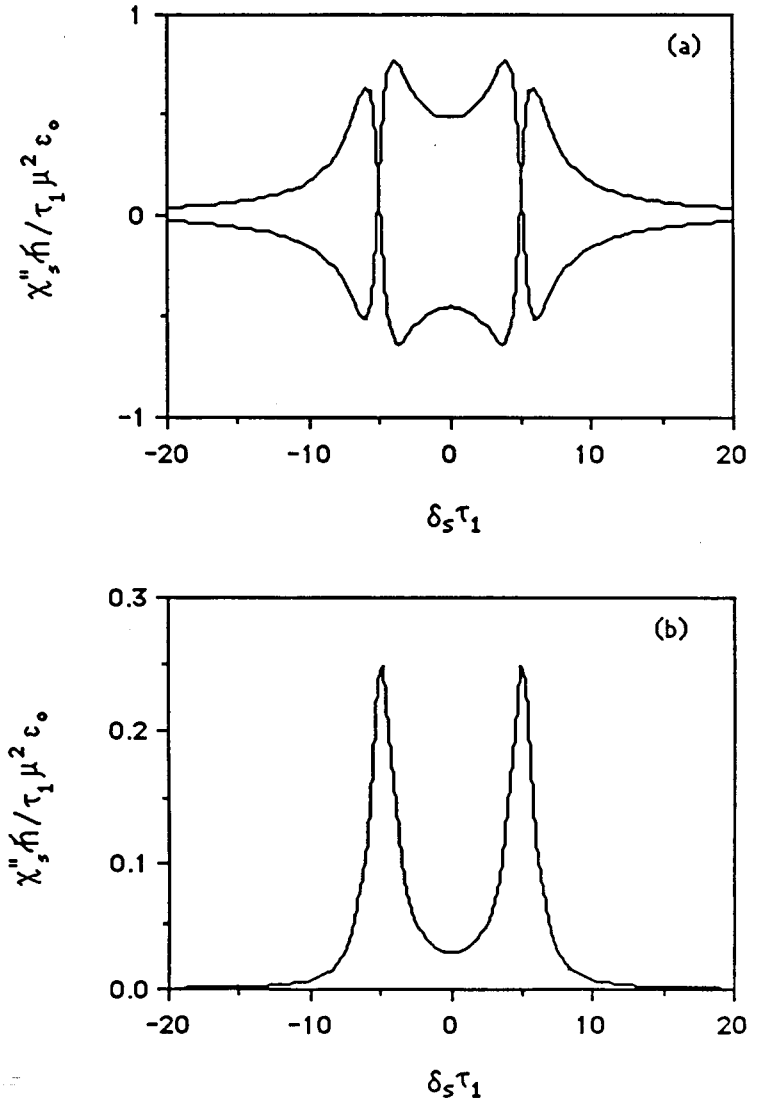
(a)
1
0
-1
-20
-10
0
10
20
$\chi''_s\hbar/\tau_1\mu^2\varepsilon_o$
$\delta_s\tau_1$
(b)
0.3
0.2
0.1
0.0
-20
-10
0
10
20
$\chi''_s\hbar/\tau_1\mu^2\varepsilon_o$
$\delta_s\tau_1$

Fig. 9

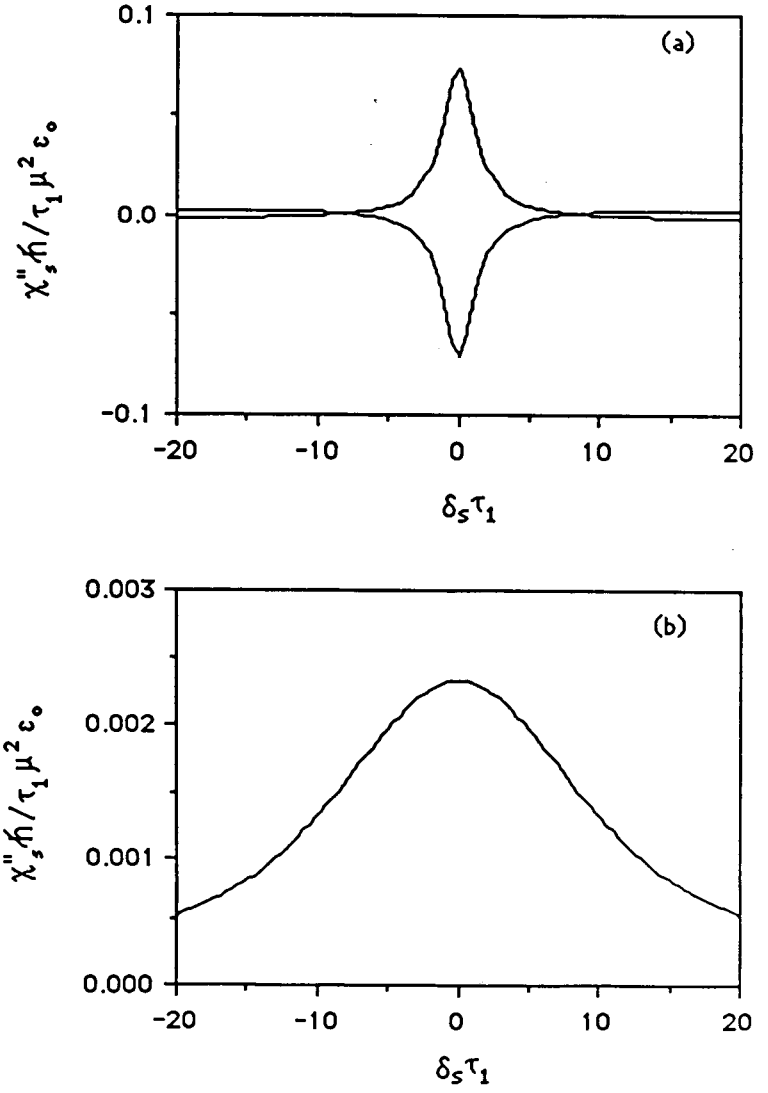
0.1
0.0
-0.1
(a)
$\chi''_s\hbar/\tau_1\mu^2\varepsilon_o$
-20
-10
0
10
20
$\delta_s\tau_1$
0.003
0.002
0.001
0.000
(b)
$\chi''_s\hbar/\tau_1\mu^2\varepsilon_o$
-20
-10
0
10
20
$\delta_s\tau_1$

Fig. 10

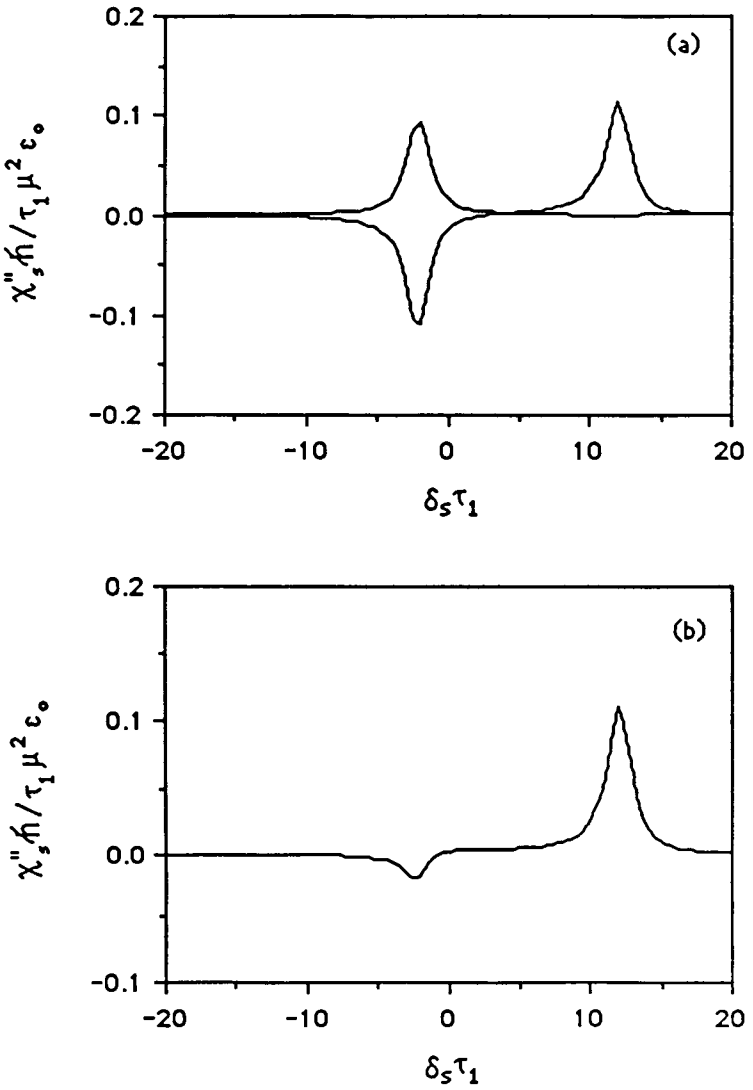
(a)
0.2
0.1
0.0
-0.1
-0.2
-20
-10
0
10
20
$\chi''_s\hbar/\tau_1\mu^2\varepsilon_o$
$\delta_s\tau_1$
(b)
0.2
0.1
0.0
-0.1
-20
-10
0
10
20
$\chi''_s\hbar/\tau_1\mu^2\varepsilon_o$
$\delta_s\tau_1$

Fig. 11

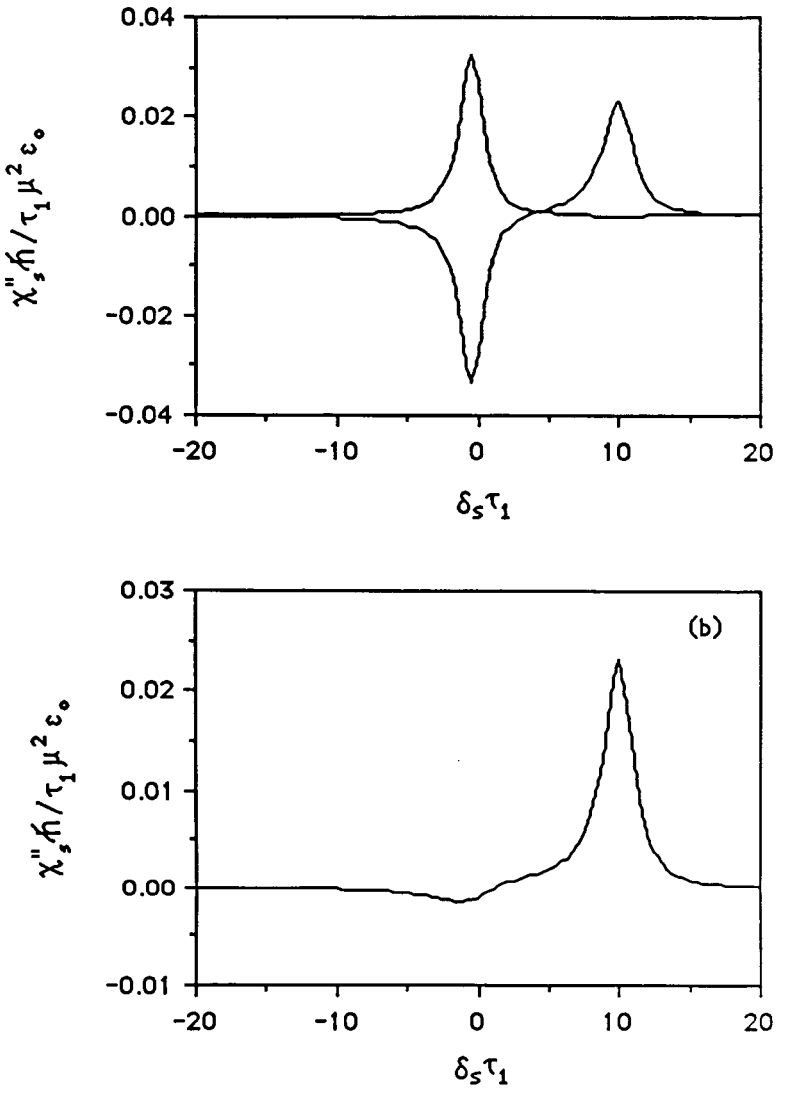
0.04
0.02
0.00
-0.02
-0.04
-20
-10
0
10
20
$\chi''_s\hbar/\tau_1\mu^2\varepsilon_o$
$\delta_s\tau_1$
0.03
0.02
0.01
0.00
-0.01
(b)
-20
-10
0
10
20
$\chi''_s\hbar/\tau_1\mu^2\varepsilon_o$
$\delta_s\tau_1$

Fig. 12

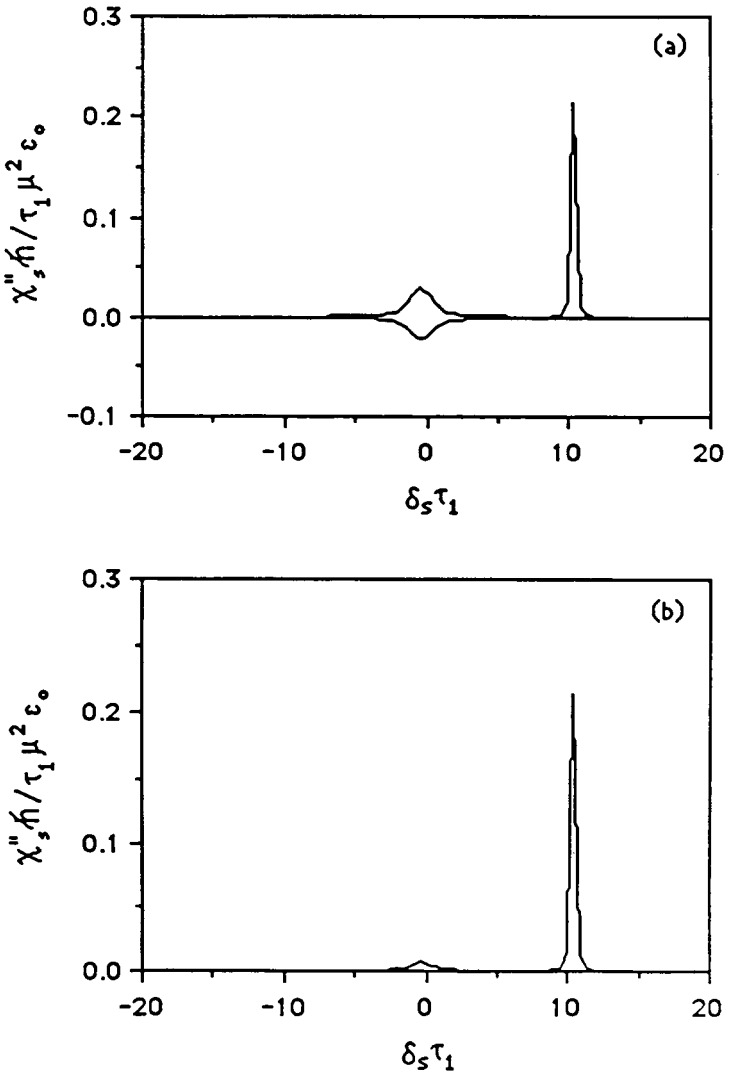
(a)
0.3
0.2
0.1
0.0
-0.1
-20
-10
0
10
20
$\chi''_s\hbar/\tau_1\mu^2\varepsilon_o$
$\delta_s\tau_1$
(b)
0.3
0.2
0.1
0.0
-20
-10
0
10
20
$\chi''_s\hbar/\tau_1\mu^2\varepsilon_o$
$\delta_s\tau_1$

Fig. 13

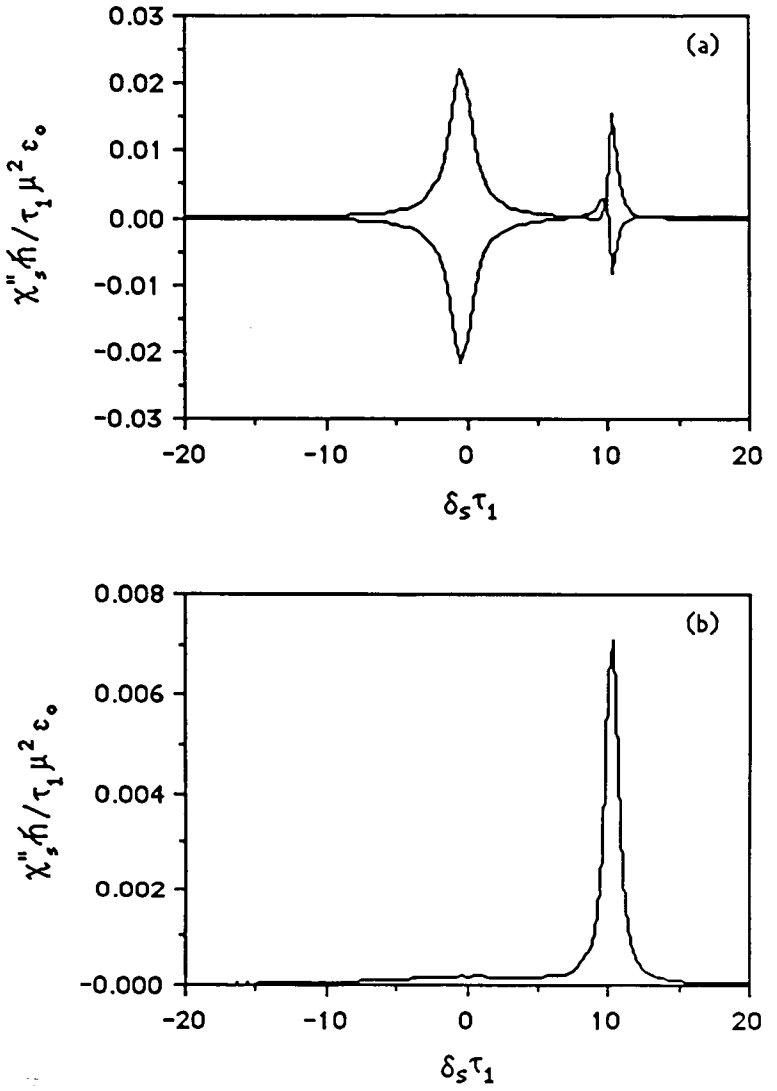
(a)
0.03
0.02
0.01
0.00
-0.01
-0.02
-0.03
-20
-10
0
10
20
$\chi''_s\hbar/\tau_1\mu^2\varepsilon_o$
$\delta_s\tau_1$
(b)
0.008
0.006
0.004
0.002
-0.000
-20
-10
0
10
20
$\chi''_s\hbar/\tau_1\mu^2\varepsilon_o$
$\delta_s\tau_1$

Fig. 14

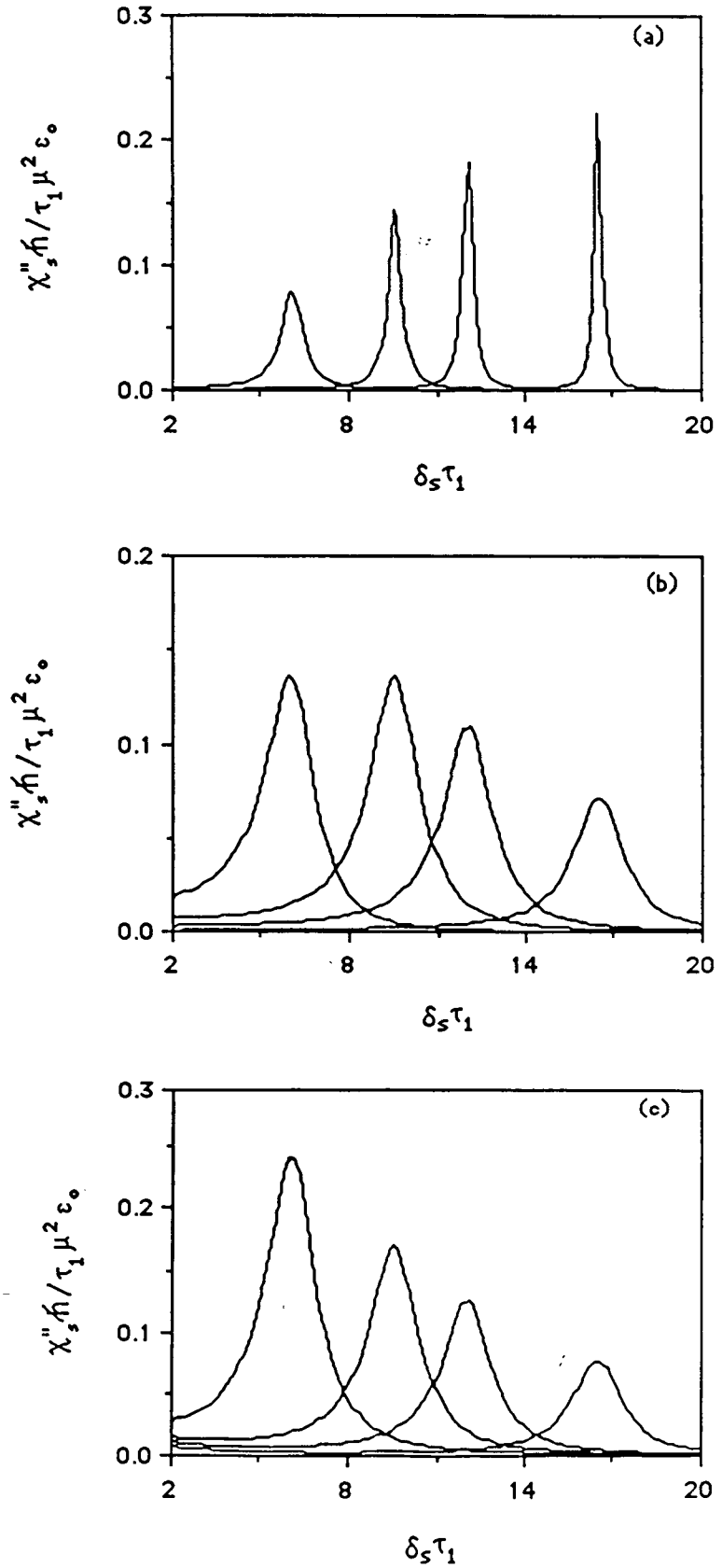
(a)
(b)
(c)
0.3
0.2
0.1
0.0
2
8
14
20
$\chi''_s\hbar/\tau_1\mu^2\varepsilon_o$
$\delta_s\tau_1$

Fig. 15

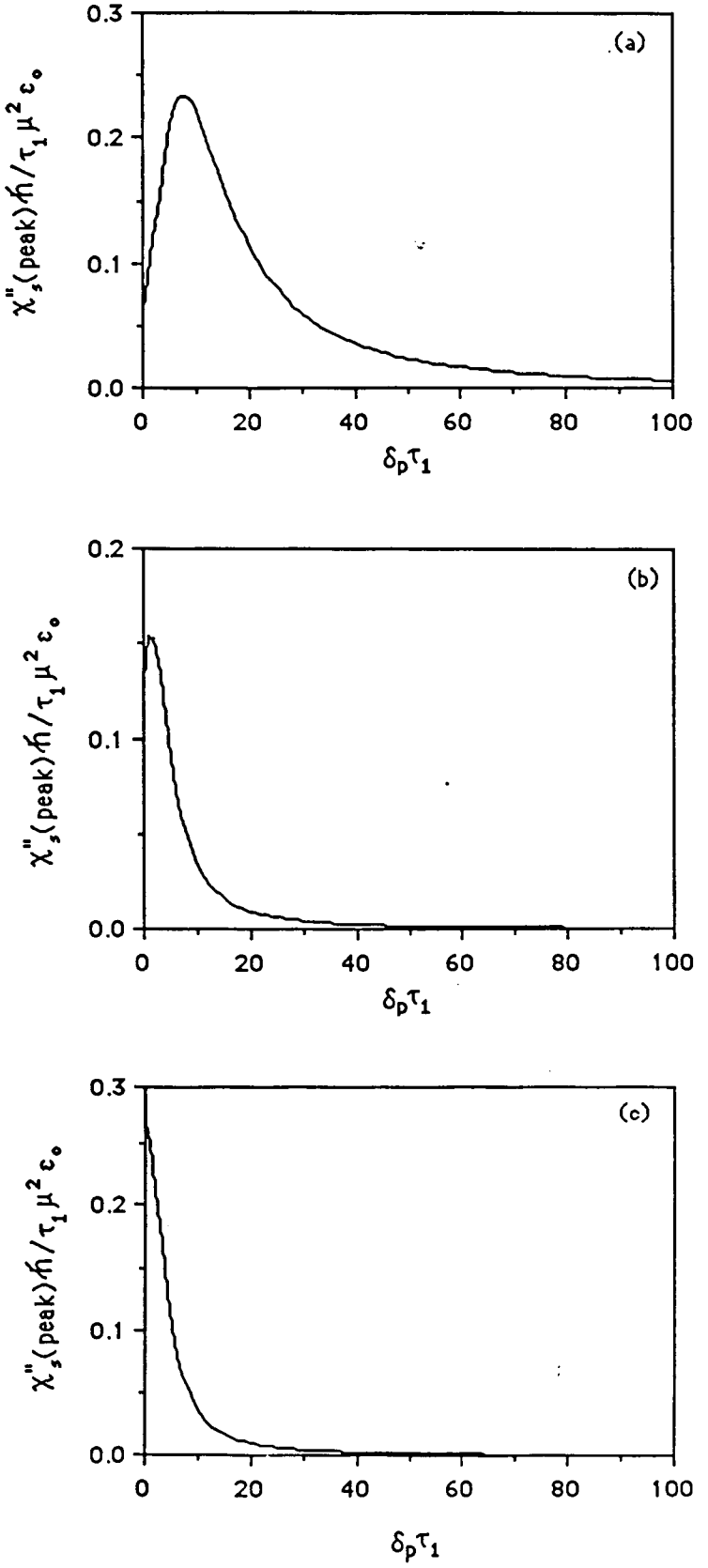
(a)
(b)
(c)
$\chi''_s(\text{peak})\hbar/\tau_1\mu^2\varepsilon_o$
$\delta_p\tau_1$
0.0
0.1
0.2
0.3
0
20
40
60
80
100

Fig. 16

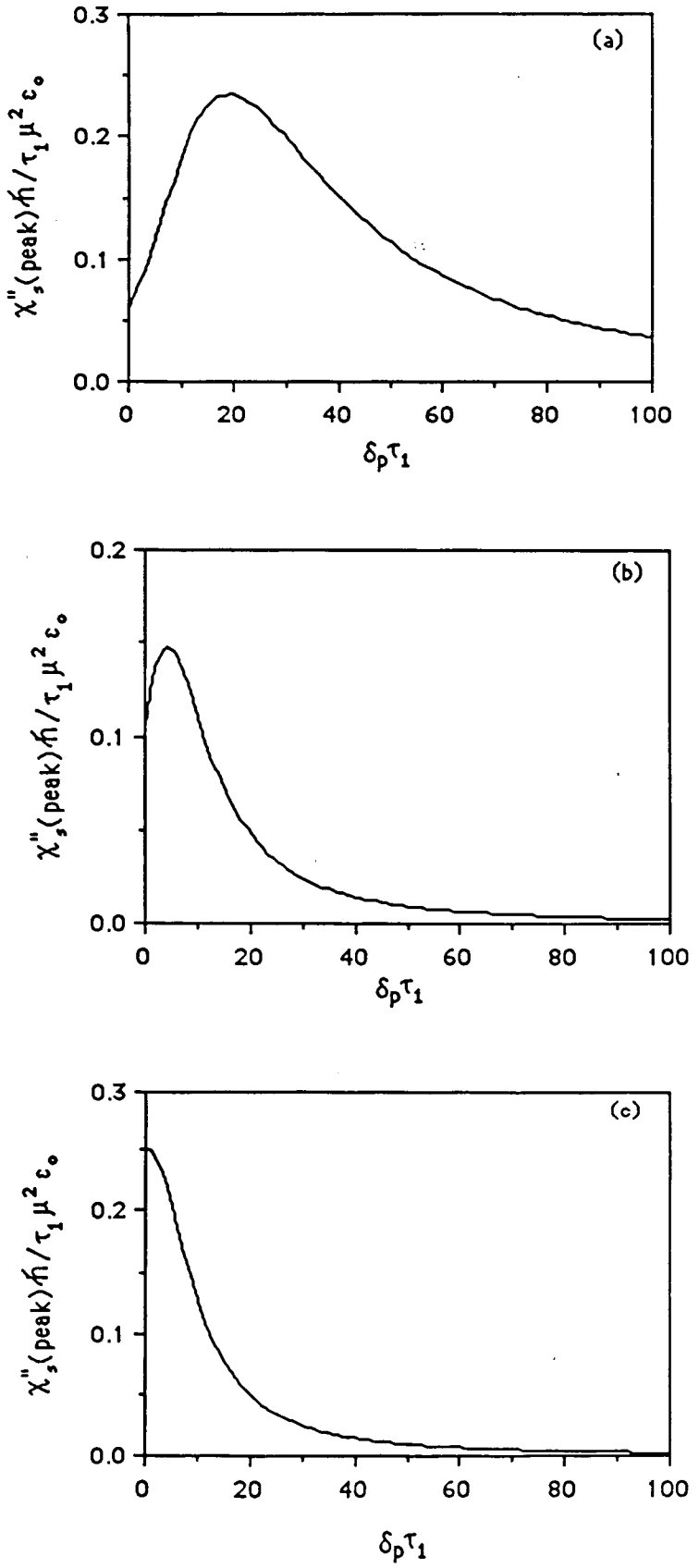
(a)
(b)
(c)
$\chi''_s(\text{peak})\hbar/\tau_1\mu^2\varepsilon_o$
$\delta_p\tau_1$
0.0
0.1
0.2
0.3
0
20
40
60
80
100

Fig. 17

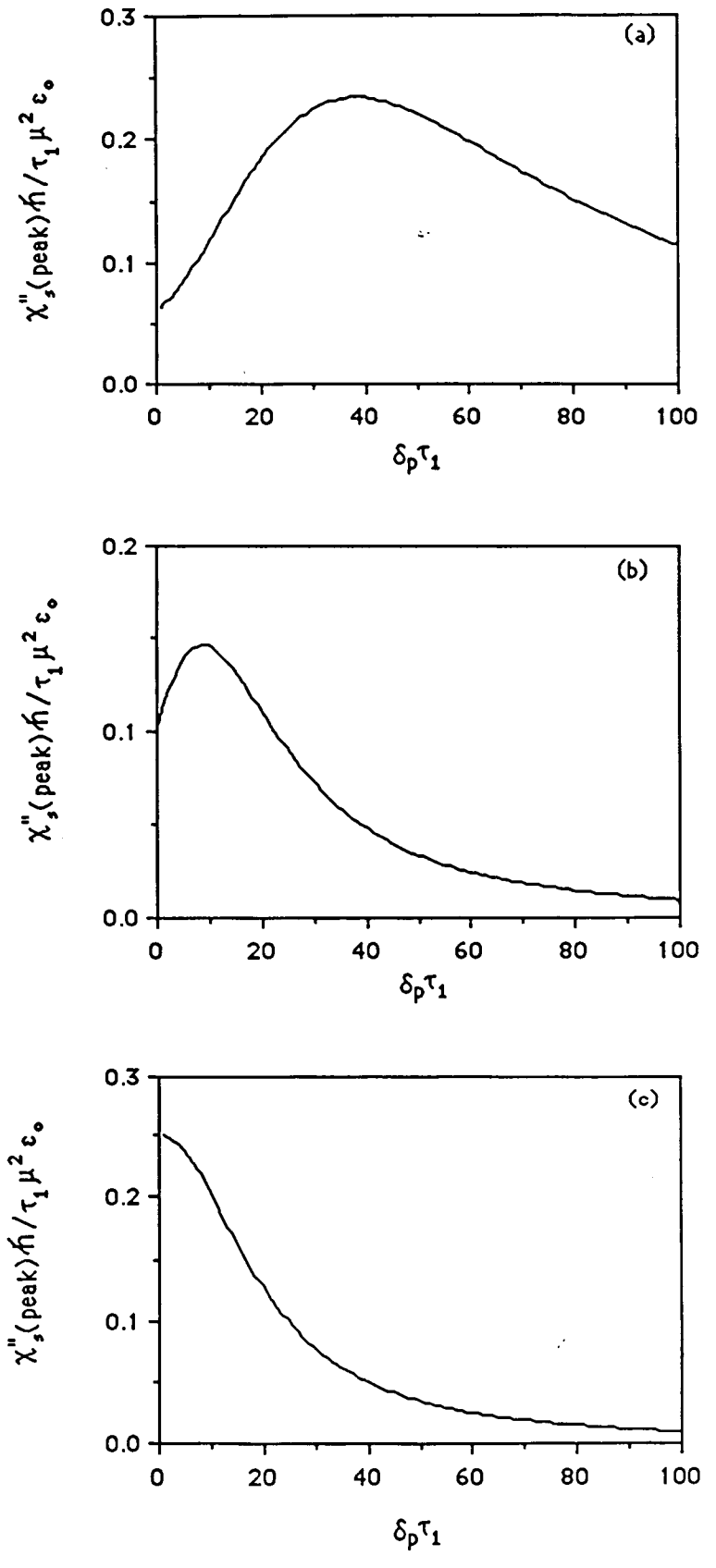
(a)
(b)
(c)
$\chi''_s(\text{peak})\hbar/\tau_1\mu^2\varepsilon_0$
$\delta_p\tau_1$
0.0
0.1
0.2
0.3
0
20
40
60
80
100

Fig.18

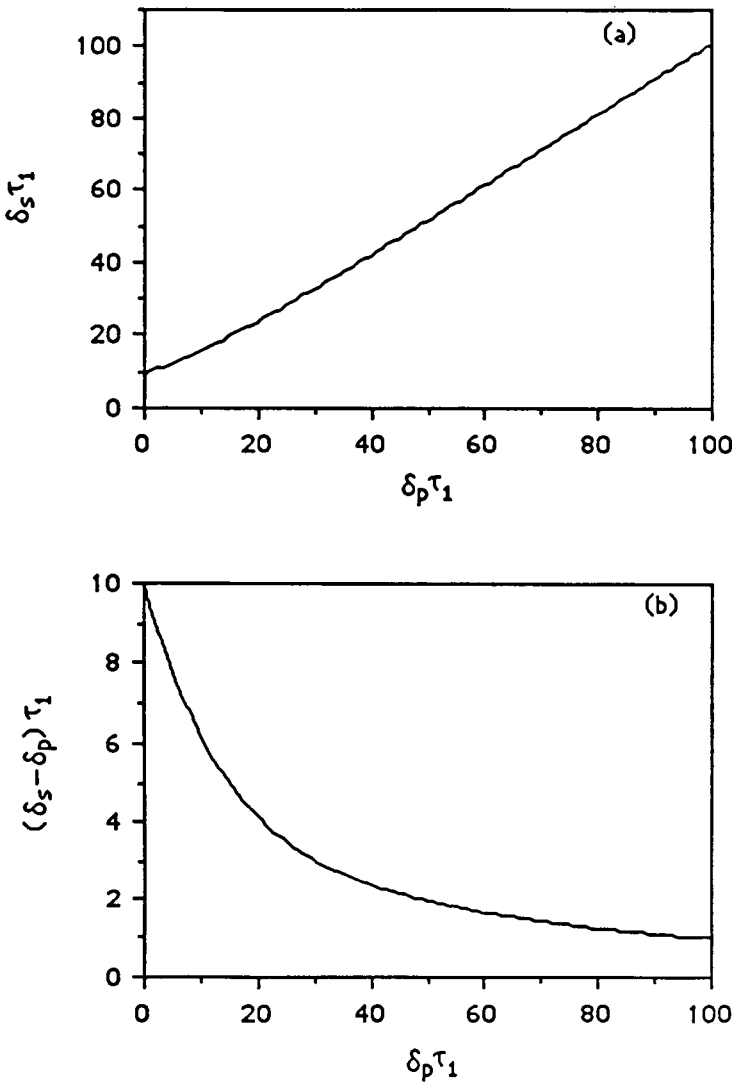
(a)
100
80
60
40
20
0
$\delta_s\tau_1$
0
20
40
60
80
100
$\delta_p\tau_1$
(b)
10
8
6
4
2
0
$(\delta_s-\delta_p)\tau_1$
0
20
40
60
80
100
$\delta_p\tau_1$

Fig. 19

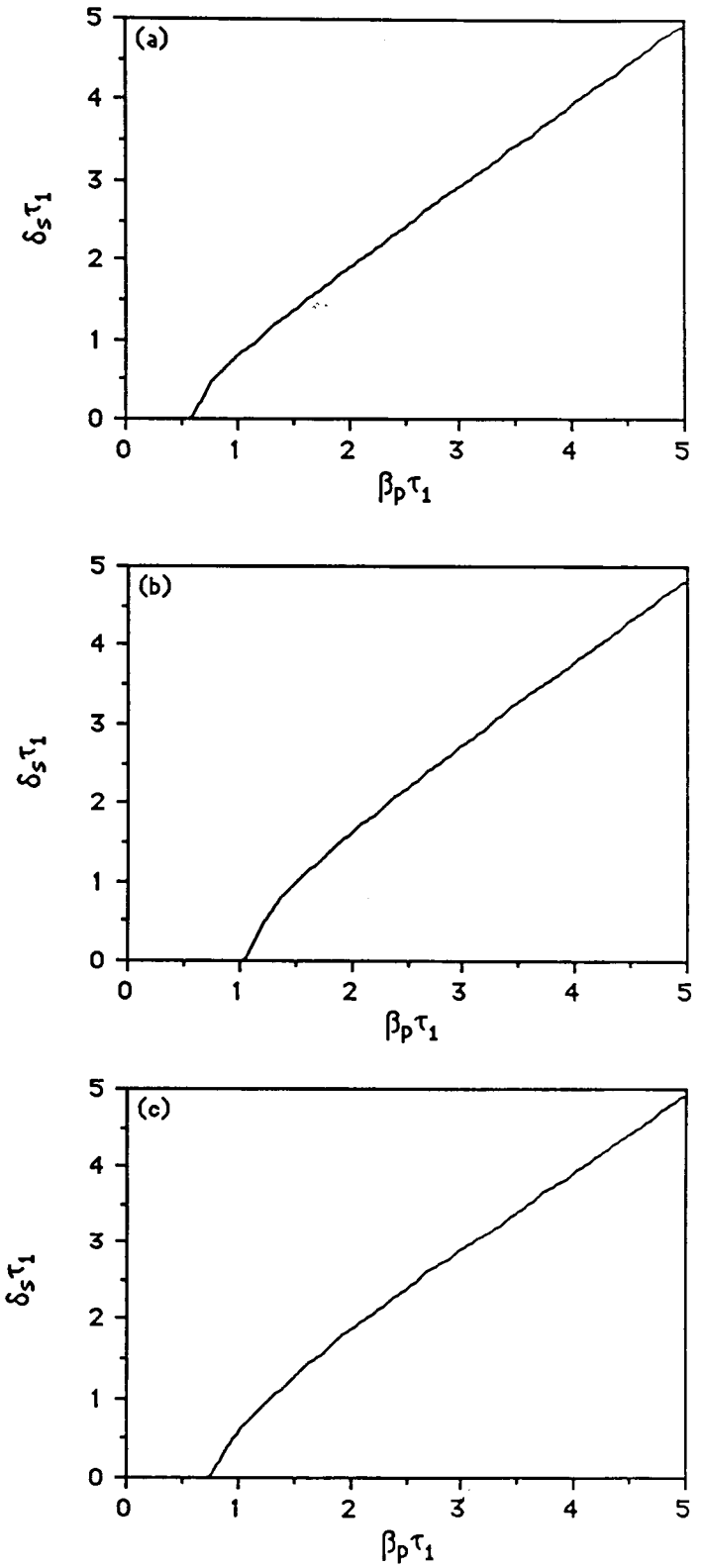

Fig. 20

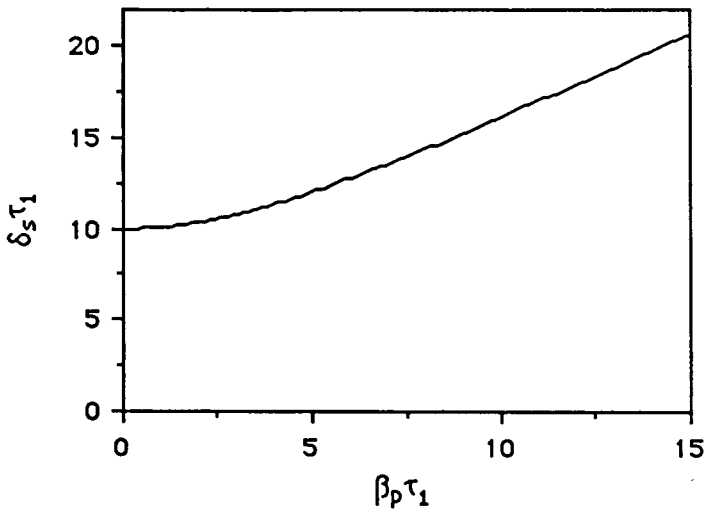

Fig. 21

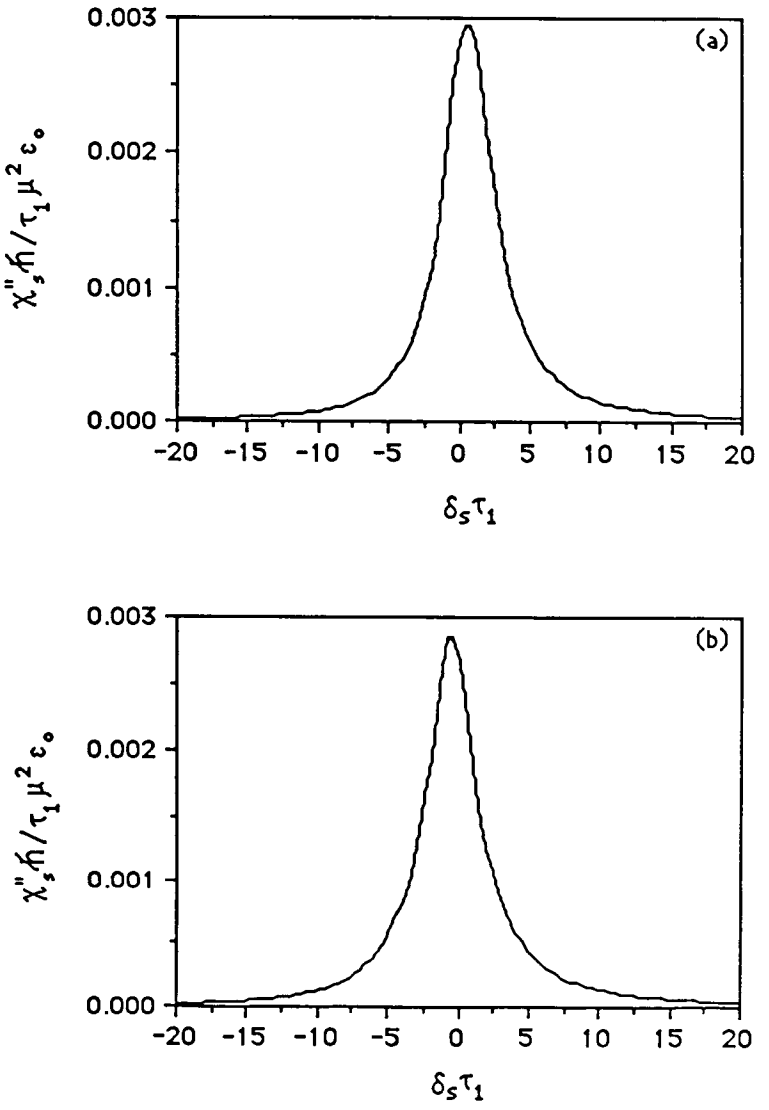
0.003
0.002
0.001
0.000
(a)
$\chi''_s\hbar/\tau_1\mu^2\varepsilon_o$
-20 -15 -10 -5 0 5 10 15 20
$\delta_s\tau_1$
0.003
0.002
0.001
0.000
(b)
$\chi''_s\hbar/\tau_1\mu^2\varepsilon_o$
-20 -15 -10 -5 0 5 10 15 20
$\delta_s\tau_1$

Fig. 22

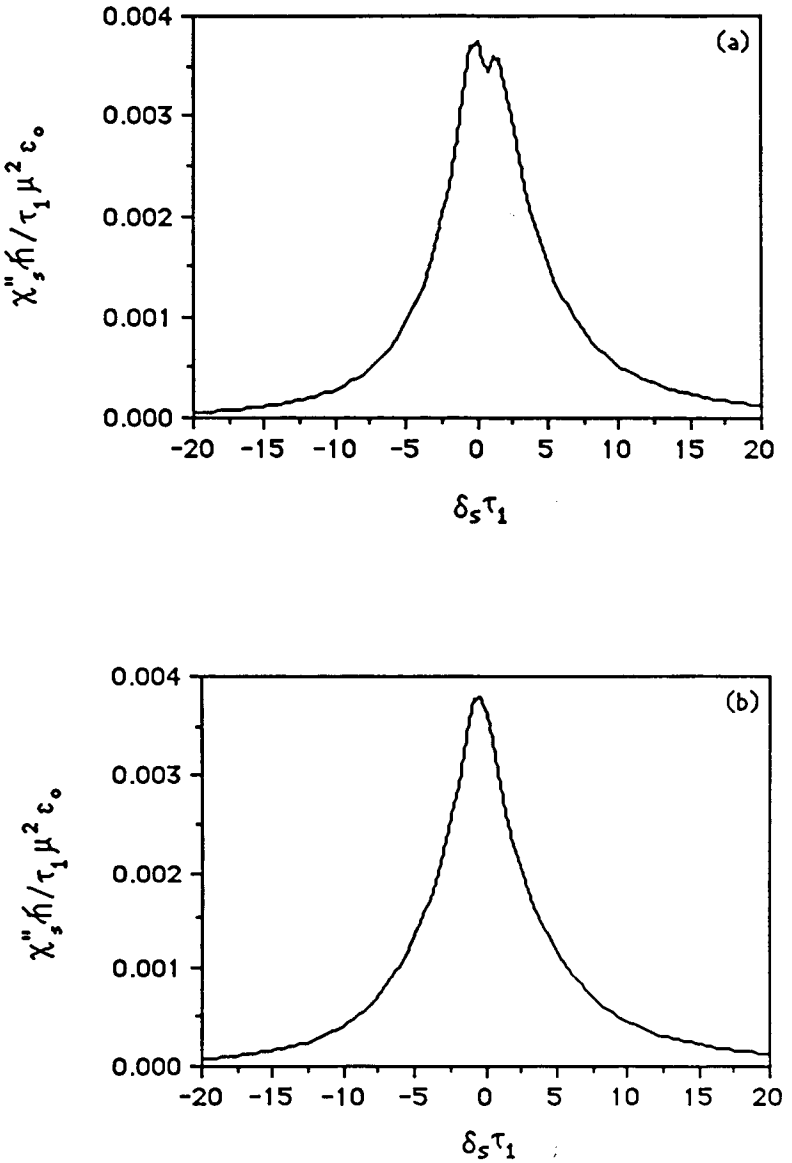
(a)
0.004
0.003
0.002
0.001
0.000
-20 -15 -10 -5 0 5 10 15 20
$\chi''_s\hbar/\tau_1\mu^2\varepsilon_o$
$\delta_s\tau_1$
(b)
0.004
0.003
0.002
0.001
0.000
-20 -15 -10 -5 0 5 10 15 20
$\chi''_s\hbar/\tau_1\mu^2\varepsilon_o$
$\delta_s\tau_1$

Fig. 23

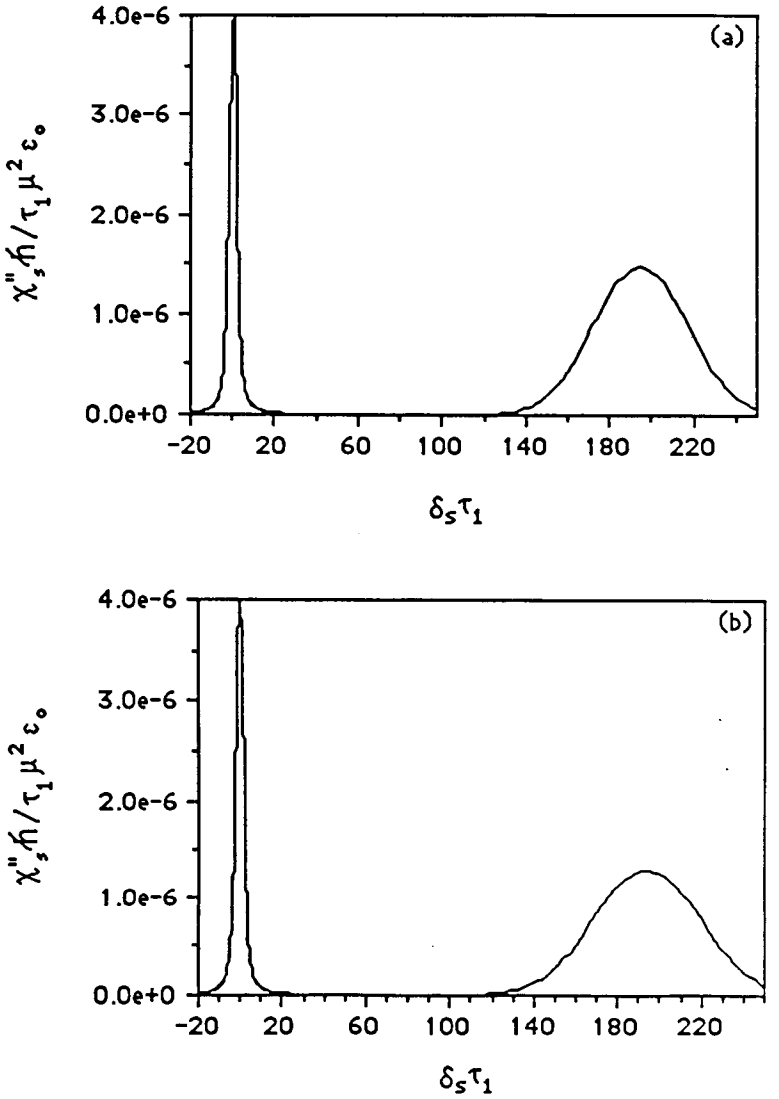
4.0e-6
3.0e-6
2.0e-6
1.0e-6
0.0e+0
(a)
$\chi''_s\hbar/\tau_1\mu^2\varepsilon_o$
-20
20
60
100
140
180
220
$\delta_s\tau_1$
4.0e-6
3.0e-6
2.0e-6
1.0e-6
0.0e+0
(b)
$\chi''_s\hbar/\tau_1\mu^2\varepsilon_o$
-20
20
60
100
140
180
220
$\delta_s\tau_1$

Fig. 24

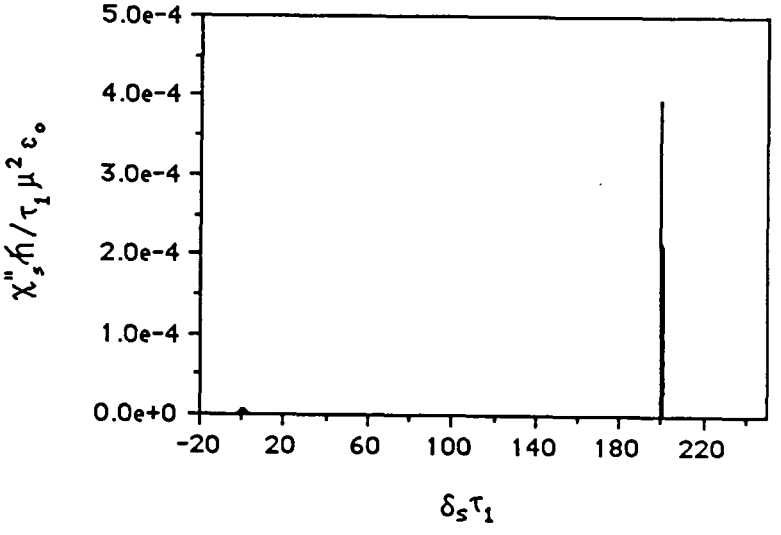
5.0e-4
4.0e-4
3.0e-4
2.0e-4
1.0e-4
0.0e+0
-20
20
60
100
140
180
220
$\chi''_s \hbar/\tau_1 \mu^2 \varepsilon_o$
$\delta_s \tau_1$

Fig. 25

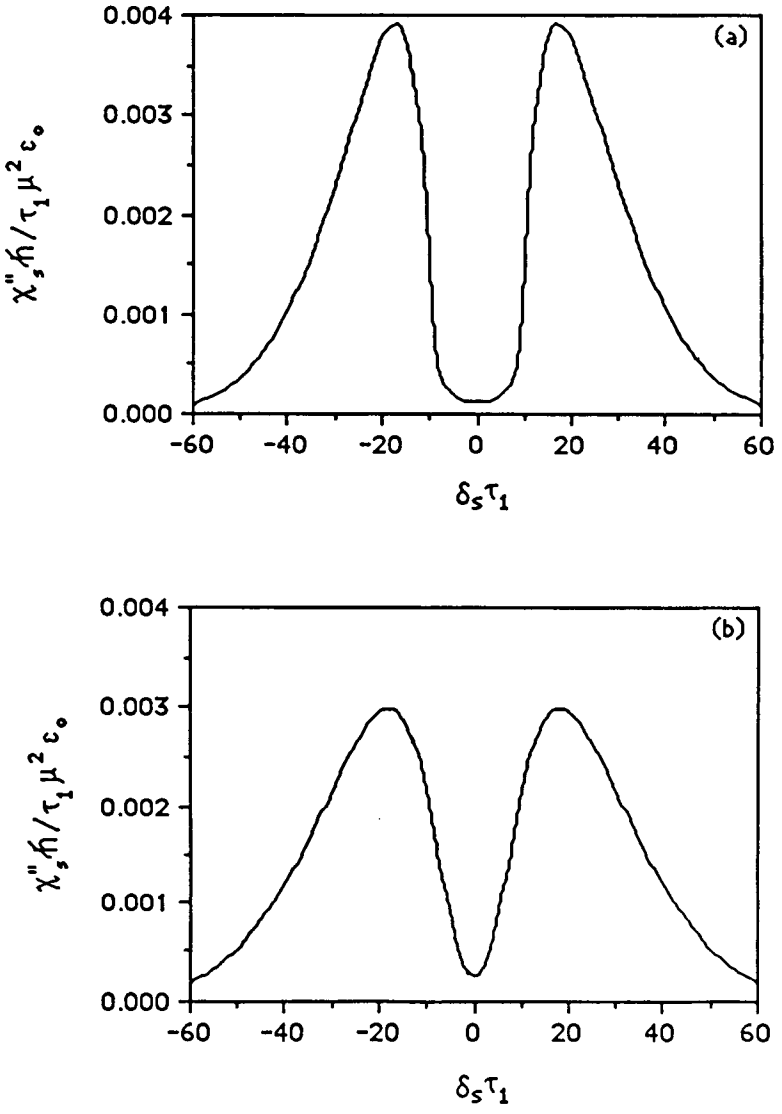
(a)
0.004
0.003
0.002
0.001
0.000
-60
-40
-20
0
20
40
60
$\chi''_s\hbar/\tau_1\mu^2\varepsilon_o$
$\delta_s\tau_1$
(b)
0.004
0.003
0.002
0.001
0.000
-60
-40
-20
0
20
40
60
$\chi''_s\hbar/\tau_1\mu^2\varepsilon_o$
$\delta_s\tau_1$

Fig. 26

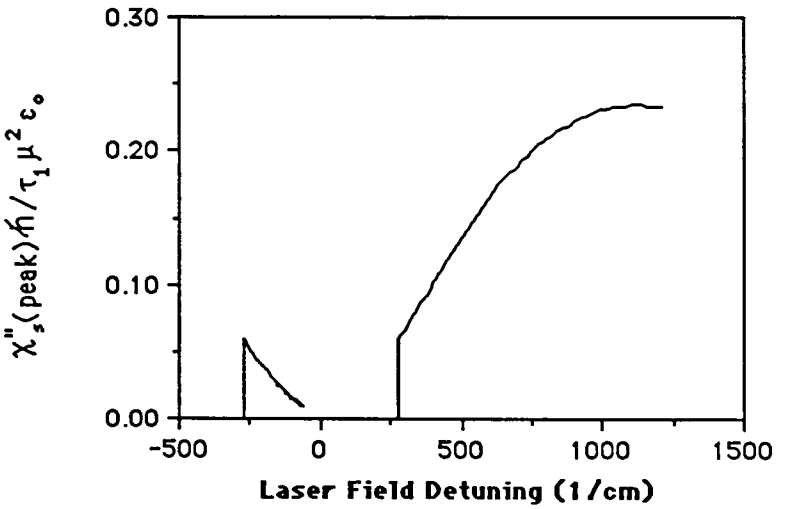
0.30
0.20
0.10
0.00
-500
0
500
1000
1500
Laser Field Detuning (1/cm)
$\chi''_s(\text{peak})\hbar/\tau_1\mu^2\varepsilon_o$

Fig. 27

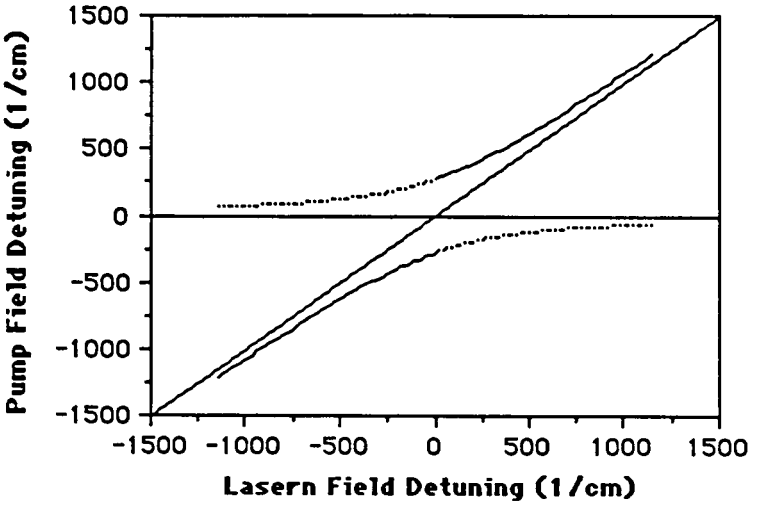
1500
1000
500
0
-500
-1000
-1500
Pump Field Detuning (1/cm)
-1500 -1000 -500 0 500 1000 1500
Lasern Field Detuning (1/cm)

Fig. 28

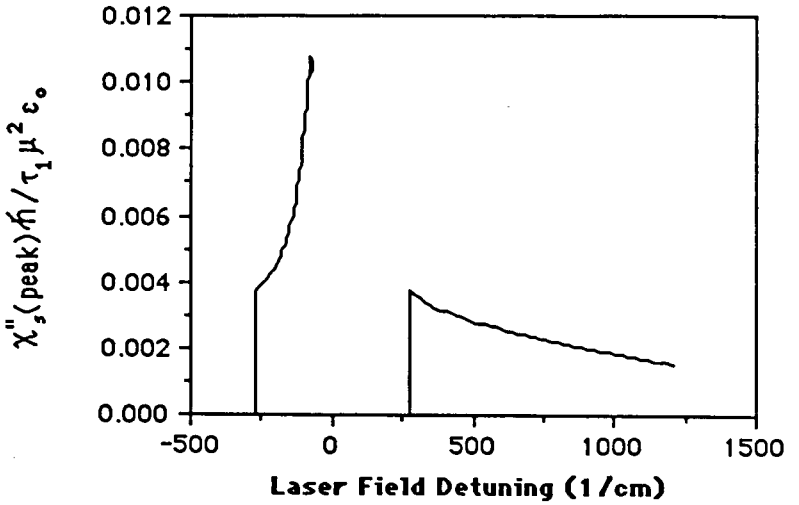
0.012
0.010
0.008
0.006
0.004
0.002
0.000
-500
0
500
1000
1500
$\chi''_s(peak)\hbar/\tau_1\mu^2\varepsilon_o$
Laser Field Detuning (1/cm)

Fig. 29